robotics

MDPI

Article

Design of a Novel Bio-Inspired Three Degrees of Freedom (3DOF) Spherical Robotic Manipulator and Its Application in Human–Robot Interactions

Suleyman Soltanov * and Rodney Roberts *

Department of Mechanical Engineering, FAMU-FSU College of Engineering, Tallahassee, FL 32310, USA
* Correspondence: ss21da@fsu.edu (S.S.); rroberts@eng.famu.fsu.edu (R.R.)

Abstract: Studying the interactions between biological organisms and their environment provides engineers with valuable insights for developing complex mechanical systems and fostering the creation of novel technological innovations. In this study, we introduce a novel bio-inspired three degrees of freedom (DOF) spherical robotic manipulator (SRM), designed to emulate the biomechanical properties observed in nature. The design utilizes the transformation of spherical Complex Spatial Kinematic Pairs (CSKPs) to synthesize bio-inspired robotic manipulators. Additionally, the use of screw theory and the Levenberg–Marquardt algorithm for kinematic parameter computation supports further advancements in human–robot interactions and simplifies control processes. The platform directly transmits motion from the motors to replicate the ball-and-socket mobility of biological joints, minimizing mechanical losses, and optimizing energy efficiency for superior spatial mobility. The proposed 3DOF SRM provides advantages including an expanded workspace, enhanced dexterity, and a lightweight, compact design. Experimental validation, conducted through SolidWorks, MATLAB, Python, and Arduino, demonstrates the versatility and broad application potential of the novel bio-inspired 3DOF SRM, positioning it as a robust solution for a wide range of robotic applications.

Keywords: bio-inspired robotics; spherical robotic manipulator; human–robot interaction; screw theory; Levenberg–Marquardt optimization

Academic Editor: Kensuke Harada

Received: 4 December 2024
Revised: 5 January 2025
Accepted: 16 January 2025
Published: 22 January 2025

Citation: Soltanov, S.; Roberts, R. Design of a Novel Bio-Inspired Three Degrees of Freedom (3DOF) Spherical Robotic Manipulator and Its Application in Human–Robot Interactions. *Robotics* **2025**, *14*, 8. https://doi.org/10.3390/robotics14020008

1. Introduction

Nature has long been an unparalleled engineer, crafting intricate body structures in humans and animals to achieve remarkable movement and adaptability. Among these designs, three degrees of freedom (3DOF) joints stand out as marvels of biomechanical ingenuity, enabling seamless interaction with complex environments. From the dexterous shoulder joint that powers human creativity to the flexible wings that carry birds across vast distances, 3DOF joints demonstrate a profound interplay of form and function.

In robotics and biomechanics, these natural designs serve as inspiration and a benchmark. The shoulder, hip, ankle, fins, and wings—each optimized for specific tasks—have provided valuable insights into developing 3DOF mechanisms and robotic systems. By studying their intricacies, researchers uncover not only the evolutionary sophistication of these systems but also pathways to replicate their adaptability in engineered models. This synthesis of biology and engineering promises breakthroughs in fields ranging from healthcare to automation, emphasizing the limitless potential of bio-inspired innovation.

Studies on 3DOF joints have extensively examined their functionality and adaptability across various body parts. For instance, Adams et al. [1] analyzed the 3DOF glenohumeral

joint in humans, emphasizing stabilizing structures, while Bakhsh & Nicandri [2] expanded on its versatile motion. Research by De Lange et al. [3] and Han et al. [4] explored wrist 3DOF, with Han focusing on rehabilitation modeling. Similarly, Molini et al. [5] and Kumar et al. [6] studied the hip joint's diagnostic potential and biomechanics. Brockett and Chapman [7] analyzed ankle 3DOF, while Pol et al. [8] addressed age-related mobility decline.

Studies on 3DOF joints in animals have highlighted significant variations in adaptability and function across species. Arias-Martorell [9] highlighted chimpanzees' flexible 3DOF shoulder joints, while Larson [10] and Larson [11] explored functional variations in gorillas and orangutans. Evans & de Lahunta [12] and Reis Silva et al. [13] examined 3DOF joints in dogs, whereas Manafzadeh [14] investigated large carnivores like lions and cheetahs. Furthermore, Bledt et al. [15] modeled these mechanics in the MIT Cheetah, while Becker et al. [16] and Böhmer et al. [17] studied joint mobility in horses, deer, and cheetahs. Brocklehurst et al. [18] explored 3DOF shoulder joints in reptiles and marsupials. Gatesy et al. [19] developed a 3DOF framework for guineafowl and alligators, expanded by Kambic et al. [20] for bipedal locomotion. Stowers et al. [21] and Baier et al. [22] linked 3DOF flight mechanics in pigeons and Chukar Partridges [23]. Similarly, Fish fin dynamics, explored by Lauder and Tangorra [24], inspired bio-robotic designs such as Sudki et al.'s [25] marine propulsor. Cortés Torres et al. [26] and Pandey et al. [27] applied 3DOF modeling to robotic fins and amphibious systems, respectively.

The initial wrist mechanism, described by Torii et al. [28], focuses on industrial robots that require powerful actuators. In contrast, Gosselin and Hamel [29] developed the Agile Eye, refined by Gosselin et al. [30], who noted motion limitations. Leguay-Durand et al. [31] enhanced dexterity with a redundant manipulator, while Vischer et al. [32] and Birglen et al. [33] focused on Argos and SHaDe, emphasizing industrial efficiency and user interaction, respectively. Innovations in surgical applications include the optimized mechanism by Lum et al. [34] and the design for space operations by Schuler et al. [35]. Compact and rigid mechanisms were developed by Yu [36] and Hess-Coelho [37], with Inada et al. [38] introducing a lightweight wrist joint and Yu et al. [39] enhancing motion smoothness. Wu et al. [40] optimized a spherical manipulator facing similar challenges as Degirmenci et al. [41] in microsurgery. Sadeqi et al. [42] focused on a hip exoskeleton, while Lee et al. [43] developed a human–machine interface to reduce interference. Li et al. [44] introduced a spherical motion generator, while Bai et al. [45] reviewed rehabilitation advances.

Hofer and D'Andrea [46] emphasized simplicity in robotic arms, contrasting with Abe et al. [47], whose ABENICS mechanism is more functional and complex. Building on specific design advancements, Rommers et al. [48] and Choi et al. [49] contributed to the development of flexure joint and microsurgical systems, respectively. Meanwhile, Howard [50] highlighted cost-effective solutions, while Ghaedrahmati and Gosselin [51] focused on wrist-gripper systems. Zhang et al. [52] developed a compact robotic wrist, with Schröder et al. [53] advancing spherical robot control. Expanding on precision, Djennane et al. [54] introduced a precise 3DOF manipulator, and Zhang et al. [55,56] focused on rehabilitation and ultrasound technologies.

Krebs et al. [57] and Pehlivan et al. [58] developed 3DOF devices for stroke rehabilitation, with a focus on wrist and forearm improvements. Expanding on assistive technologies, Fite et al. [59] and Fan et al. [60] created prosthetics, with Fite's gas-actuated arm offering more DOF and Fan's wrist prosthetic covering most daily tasks. Amirabdollahian et al. [61] and Singh et al. [62] both targeted home-based stroke rehabilitation, while Jarrassé et al. [63] and Rose et al. [64] focused on transparency in human–robot interactions. Pezent et al. [65] improved RiceWrist-S ergonomics, and Bajaj et al. [66] emphasized dexterity in wrist mechanisms. Extending rehabilitation robotics to the lower limbs, Li et al. [67] introduced

an ankle rehab robot, and Vertongen et al. [68] reviewed lightweight prosthetic systems. Specifically, Eschweiler et al. [69] examined wrist biomechanics for clinical use.

Soltanov et al. [70–72] contributed to the structural synthesis of robot manipulators, improving dynamic performance, motion control, and design for industrial and medical applications. Yousaf et al. [73] and Amal et al. [74] explored bioinspired designs in MAVs and marine robotics, respectively. Morgansen et al. [75] and Kim et al. [76] developed bioinspired underwater robots, focusing on efficient mobility, like Li et al. [77] with a biomimetic pectoral fin. Focusing on human–robot interactions, Wyrobek et al. [78] and Mahmoud et al. [79] developed modular and safety-oriented robotic systems, while Chernyak et al. [80] and Bright et al. [81] focused on quadrupedal and cheetah-inspired robots for rough terrain and speed. Hammond et al. [82] and Hu et al. [83] designed precision wrists for medical applications, while Hwang et al. [84] and Hernández-Flores et al. [85] improved adaptive control in surgical and quadrupedal robots. Kuka AG [86] and Selvamuthu et al. [87] advanced precision robotics for industrial and robotic arm applications.

In this study, we present the design and development of a novel bio-inspired 3DOF SRM with advanced spatial mobility, capable of replicating the functional characteristics of a 3DOF joint observed in biological organisms. The proposed 3DOF SRM offers significant improvements over existing systems, including an expanded workspace, enhanced dexterity, and a lightweight, compact form factor. These features make the manipulator a versatile solution for various applications, including medicine, industrial automation, aerospace, robotics, consumer electronics, and defense.

In the preliminary phase of our research, we focused on human–robot interactions, particularly examining the human hand's medical functionality and the hand–eye coordination process. In the subsequent phase, we applied the transformation of spherical CSKPs to systematically synthesize the 3DOF SRM and determine its mobility number. Furthermore, we employed the screw theory and Levenberg–Marquardt optimization to solve both forward and inverse kinematics of the 3DOF SRM, ensuring precise motion control and high maneuverability. The design is realized by 3D printing the 3DOF SRM's components, followed by assembly and comprehensive experimental evaluation. In the final phase of the study, the exploration of the human–robot interaction is integrated into the 3DOF SRM as a wrist joint, leading to a more refined and efficient control system that transitions from passive perception to active control through manipulation, thereby enhancing its operational performance. The results are analyzed to validate the performance of the manipulator, demonstrating its potential for widespread application in various technical domains.

2. The Anatomy of the Human Arm and Its Implications for Robot Interaction

The human arm is an intricate and sophisticated system composed of bones, muscles, tendons, and nerves that work together seamlessly to facilitate a vast range of motion and enable interaction with the environment. In order to design robotic manipulators that can perform tasks similar to those carried out by humans, it is crucial to have a comprehensive understanding of the anatomy of the human arm.

The human arm has a wide range of mobility, including flexion (bending), abduction (moving away from the body's midline), medial rotation (inward rotation), lateral rotation (outward rotation), extension (straightening), pronation (turning the palm down), supination (turning the palm up), and combinations of flexion/abduction and abduction/extension [88] (Figure 1). Among this system, the wrist joint permits movement in the spherical coordinate system, which includes flexion and extension, radial and ulnar deviation, and pronation and supination. Therefore, as a result of our extensive research, we

have developed a novel bio-inspired 3DOF SRM that is capable of mimicking the mobility of the human wrist joint by using the method of transformation of spherical CSKPs.

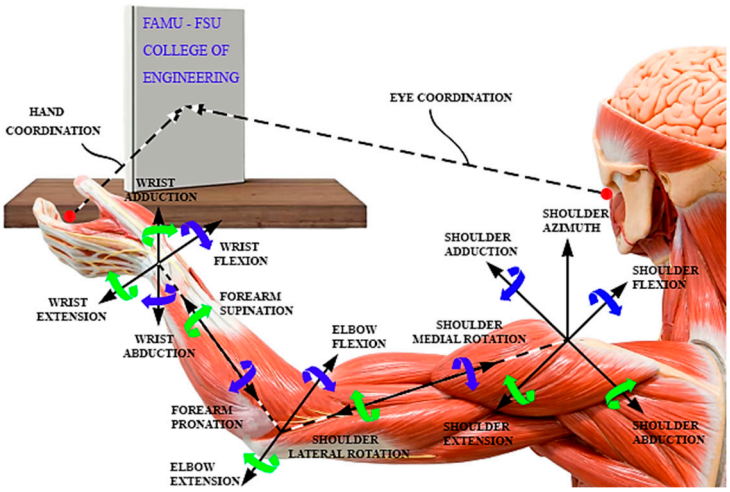

Figure 1. The depiction of human arm kinematic mobility and hand–eye coordination in human–object interaction. The blue and green arrows represent shoulder, elbow, and wrist movements along their axes of rotation. Dashed lines depict hand-eye coordination pathways.

Manipulating an object allows us to modify our environment and serve as a crucial connection to the external world. It involves not only physical factors but also anticipating future outcomes. For example, when reaching for a book, visual attention shifts to coordinate motor actions, guided by sensorimotor and visual feedback. The hand approaches the object, adjusts its orientation, and closes around it. Tactile signals confirm contact, and any deviation prompts immediate corrective adjustments to achieve the intended outcome. We often adapt our initial approach for end-state comfort [89], a skill that develops over time. Experience also helps us handle fragile, hazardous objects, or handovers [90], guided by prior knowledge and the action's intended purpose.

Dexterous manipulation follows a consistent hand-arm kinematic pattern, where hand aperture peaks according to object size before closing upon contact, as observed by Jeannerod [91] and confirmed in further studies exploring other object and kinematic factors. However, individuals with neurological conditions like Dyspraxia or Developmental Coordination Disorder (DCD) experience difficulty in planning and executing movements [92]. This impairment in hand–eye coordination often results in challenges during object interactions, such as unintentional dropping or breakage. The eyes must accurately assess distance and object placement during movement, which can be especially difficult for individuals with DCD (Figure 1).

Consequently, the second phase of our research focuses on simplifying the control system of the novel bio-inspired 3DOF SRM, enhancing precision and reliability in object manipulation.

3. Design and Methodology of the Novel Bio-Inspired 3DOF SRM

This section systematically outlines the development of a novel class of robotic manipulators, emphasizing the transition from conceptual to analytical design principles. The research involves structural synthesis by examining the interactions between geometric entities and their transformation into robotic manipulators. Our current focus is on designing a bio-inspired 3DOF SRM, where the end effector's motion is mapped within a spherical coordinate system. A key aspect of this design process is the analysis of the end effector's movement trajectory, which necessitates a thorough investigation of the mobility within spherical CSKPs.

In this context, the mobility of two concentric spheres depicted in Figure 2a serves as a fundamental spherical CSKPs. A sphere with center O2 and radius r is positioned concentrically within a fixed sphere of center O1 and radius R, forming a system with 3DOF. This connection is exemplified in biological organisms by the ball and socket joint. These DOFs correspond to rotational motions about the x, y, and z axes, represented by the angles α, β, and γ, respectively, thereby constituting a higher-order kinematic pair. By establishing a spherical coordinate system on sphere 2, the motion equation for any point, P, on this sphere relative to sphere 1 can be determined, facilitating the precise control and movement of the end effector within the spherical coordinate system.

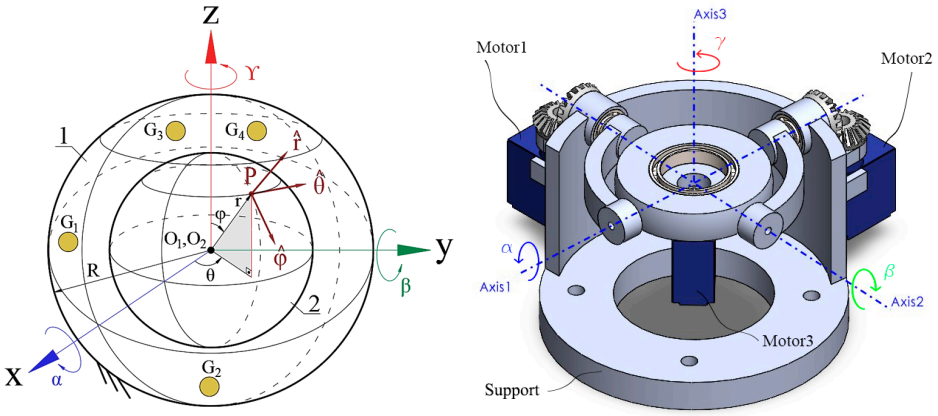

Figure 2. (**a**) The mutual concentric configuration of the fixed sphere 1, with center $O1$ and radius R, and sphere 2, with center $O2$ and radius r. (**b**) A novel bio-inspired constrained 3DOF SRM derived from the transformation of the spherical CSKPs.

The platform of the novel 3DOF SRM, structurally synthesized from the transformation of the spherical CSKPs, exhibits the same spatial mobility, denoted as $\{\lambda_i\}_1^3$, as sphere 2. In the design of this novel bio-inspired 3DOF SRM, we employ revolute kinematic pairs along each coordinate axis (Axis1, Axis2, Axis3) to achieve the desired spherical motion. These revolute joints drive the arms, which function as the generator of the spheres, maneuvering the mobile platform relative to the fixed reference frame of sphere 1, which serves as the support in Figure 2b. Furthermore, it is feasible to select the grounding points (G_1, G2, G3, G_4) for the novel 3DOF SRM at any arbitrary location on the stationary sphere 1, providing flexibility in the system's configuration.

To determine the mobility and kinematic parameters of the mobile platform in the novel bio-inspired constrained 3DOF SRM, it is essential to analyze the mobility and kinematics of the spherical CSKPs for the specified configuration. The rotational motion of the spherical CSKPs about the x and y axes can be represented using the rotation matrices $R_x(\alpha)$ and $R_y(\beta)$, as shown in Equation (1).

$$R_x(\alpha) = \begin{bmatrix} 1 & 0 & 0 \\ 0 & \cos(\alpha) & -\sin(\alpha) \\ 0 & \sin(\alpha) & \cos(\alpha) \end{bmatrix}, \; R_y(\beta) = \begin{bmatrix} \cos(\beta) & 0 & \sin(\beta) \\ 0 & 1 & 0 \\ -\sin(\beta) & 0 & \cos(\beta) \end{bmatrix} \tag{1}$$

where the angles α and β represent the rotations about the x and y axes, respectively. To achieve simultaneous rotation about both axes, the product of the $R_x(\alpha)$ and $R_y(\beta)$ matrices must be defined, as shown in Equation (2).

$$T = R_x(\alpha)R_y(\beta) = \begin{bmatrix} \cos(\beta) & 0 & \sin(\beta) \\ \sin(\alpha)\sin(\beta) & \cos(\alpha) & -\cos(\beta)\sin(\alpha) \\ -\cos(\alpha)\sin(\beta) & \sin(\alpha) & \cos(\alpha)\cos(\beta) \end{bmatrix} \tag{2}$$

This transformation matrix, T, represents the combined rotational motion around the x and y coordinate axes at angles α and β. If we attempt to rotate the sphere simultaneously along both axes, the result is a rotation around a diagonal axis passing through the sphere's center. This outcome is explained by Euler's rotation theorem, which states that any arbitrary rotation can be represented as a single rotation around a unique axis [93]. Therefore, under the given conditions, it is impossible to achieve independent rotations along both the x and y axes simultaneously with a fixed center point.

The kinematic parameters of the novel bio-inspired constrained 3DOF SRM's mobile platform are obtained in the next step by applying the transformation matrix (T) on the spherical CSKPs to the selected central coordinate origin and point (P) with radius r. To represent a point, P, on sphere 2, we can utilize spherical coordinates ($r,\ \varphi,\ \theta$), where the polar angle (measured from the positive z-axis) is represented by φ and the azimuth angle (measured from the positive x-axis) is represented by θ (Figure 2a). To obtain the kinematic parameters, we need to convert the given spherical coordinates into Cartesian coordinates (x, y, z) using the following Formula (3):

$$\begin{cases} x = rsin(\theta)cos(\varphi) \\ y = rsin(\theta)sin(\varphi) \\ z = rcos(\theta) \end{cases} \tag{3}$$

In the subsequent stage, we can calculate the position vector (P_{xyz}) of the point, P, after rotation by multiplying the transformation matrix (T) with the transformed coordinates (3), which can be expressed as follows (4):

$$P_{xyz} = T \begin{bmatrix} x \\ y \\ z \end{bmatrix} = \begin{bmatrix} rs(\beta)c(\theta) + rc(\beta)c(\varphi)s(\theta) \\ rc(\alpha)s(\varphi)s(\theta) - rc(\beta)s(\alpha)c(\theta) + rc(\varphi)s(\alpha)s(\beta)s(\theta) \\ rc(\alpha)c(\beta)c(\theta) + rs(\alpha)s(\varphi)s(\theta) - rc(\alpha)c(\varphi)s(\beta)s(\theta) \end{bmatrix} \tag{4}$$

The P_{xyz} matrix (4) obtained will serve to characterize the displacement of the mobile platform for any given instant of time in the novel bio-inspired constrained 3DOF SRM. The matrix P_{xyz} will consist of post-rotation state vectors of the point, P, for each row element, where the state vectors correspond to the coordinates xt, yt, and zt. We can consider the parameters θ and φ of the spherical coordinate system, placed in the spherical CSKPs, as constant, while the parameter, r, can be defined as the synthesis parameter and remains variable. The Jacobian matrix (J) is used to determine the linear velocity of point P on sphere 2 and the mobile platform simultaneously, as shown in Equation (5).

$$J = \mathrm{T}R_z(\varphi)R_y(\theta) \begin{bmatrix} 0 & -c(\beta)s(\varphi) & c(\varphi) \\ 0 & s(\beta)s(\theta) - c(\beta)c(\varphi)c(\theta) & -s(\varphi)c(\theta) \\ 1 & 0 & 0 \end{bmatrix} \begin{bmatrix} 1 & 0 & 0 \\ 0 & r & 0 \\ 0 & 0 & r \end{bmatrix} \tag{5}$$

The matrix J (5) contains linear velocity vectors of point, P, after rotation along the x, y, and z axes represented by Vxt, Vyt, and Vzt, respectively. The term R is excluded from Equation (5) because the Jacobian matrix concerns the linear velocity of the mobile platform, with the stationary sphere acting as a fixed reference point. The determinant of the Jacobian matrix is utilized to extract valuable information regarding the kinematic behavior of the designed novel bio-inspired constrained 3DOF SRM (6), including singular configuration, volume expansion, and contraction. The relationship between the kinematic and geometric parameters of the novel bio-inspired constrained 3DOF SRM is established through the determinant, which defines the motion of the moving sphere 2 relative to

the fixed sphere 1 as a scaling factor, represented by the ratio r/R (where $R = 1$ in this particular case), capturing the interaction between these parameters.

$$\det(J) = ratio^2(c(\beta)c(\theta) - s(\beta)c(\varphi)s(\theta)) \tag{6}$$

Formula (7) is used to determine the angular velocity of the point, P, on both sphere 2 and the mobile platform simultaneously.

$$\omega = J^{-1}\begin{bmatrix} Vxt \\ Vyt \\ Vzt \end{bmatrix} \tag{7}$$

Each row element ωxt, ωyt, and ωzt of the obtained ω matrix (7) will be the post-rotation angular velocity vectors of the point, P, respectively. As a result, the kinematic parameters, such as displacement, linear velocity, and angular velocity of the mobile platform of the novel bio-inspired constrained 3DOF SRM, can be determined using Formulas (4), (5) and (7) for any selected point on it.

Equation (8) demonstrates the representation of a rigid body's velocity (sphere 2 or moving platform) as a point in $\mathbb{R}^6$ by utilizing a spatial velocity or twists (V_{twist}), which is a combination of three angular and three linear velocities.

$$V_{twist} = \begin{bmatrix} \omega xt & \omega yt & \omega zt \\ Vxt & Vyt & Vzt \end{bmatrix} \in \mathbb{R}^6 \tag{8}$$

Based on the geometric and mathematical analysis conducted, it has been determined that the mobility of the mobile platform in the novel bio-inspired constrained 3DOF SRM, designed by transforming the spherical CSKPs mirrors the spatial mobility of the spherical CSKPs. Consequently, the spatial mobility, denoted as $\{\lambda_i\}_1^3$, can be established through a defined process: first, rotating one arm around a chosen coordinate axis ($Axis1$) and returning it to its original position, followed by the rotation of the second arm ($Axis2$) in a similar manner. Additionally, the mobile platform of the novel bio-inspired constrained 3DOF SRM can perform unrestricted rotational motion (γ) around the z-axis ($Axis3$) at any spatial position. This constrained configuration is well-suited for applications where spherical arms and the body are subjected to high loads, such as in robotic arms or legs undergoing heavy weight-bearing, rocket maneuvers, or bio-inspired underwater robotic systems. It helps prevent motor overload, ensuring reliable and efficient operation under demanding conditions.

To achieve smooth 3DOF motion of the mobile platform within a spherical space and to eliminate the joint constraint in the novel bio-inspired constrained 3DOF SRM (as illustrated in Figure 2b), two movable spherical platforms are introduced by releasing one of the spherical arms (previously fixed sphere1). Figure 3a demonstrates the newly designed bio-inspired 3DOF SRM, which mimics the ball and socket joint movement observed in biological systems, as shown in Figure 3b.

Through our research process, we have formulated and presented the following three axioms, which establish a foundational basis for developing this type of novel bio-inspired robotic manipulator.

Axiom 1: Kinematic pairs that converge at a point, line, or surface, based on theoretical geometric parameters such as coordinate systems, angles of rotation, planes of symmetry, or imaginary axes within spatial configurations, are classified as Complex Spatial Kinematic Pairs (CSKPs).

Axiom 2: By selecting supports on the kinematic pairs that form Complex Spatial Kinematic Pairs, a mobile platform can be created with the same degree of freedom as those kinematic pairs.

Axiom 3: The kinematic parameters of the end effector in the robotic manipulator, developed through the transformation of Complex Spatial Kinematic Pairs, will reflect the kinematic parameters inherent to those kinematic pairs.

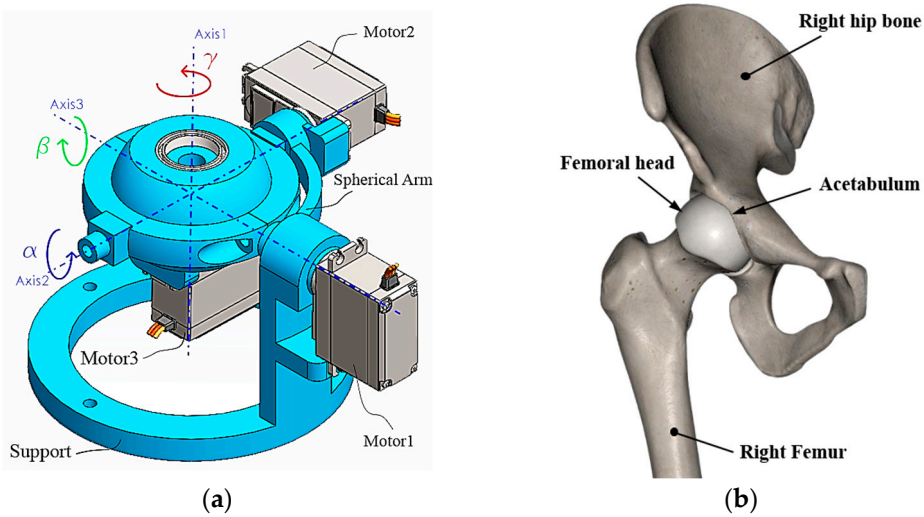

(**a**) (**b**)

Figure 3. (**a**) A novel bio-inspired 3DOF SRM designed from the transformation of spherical CSKPs. (**b**) Anatomical illustration of the human right hip joint, highlighting the ball and socket connection between the femoral head and acetabulum.

The novel bio-inspired 3DOF SRM, illustrated in Figure 3a, features a sequential configuration, where the number of revolute pairs ($\sum_{i=1}^{j} f_i = 3$) directly corresponds to its degree of freedom ($M = 3$). At this stage, the motion is directly transmitted from the motors to the spherical arms and the mobile platform of the novel bio-inspired 3DOF SRM, minimizing slippage, wear, and the number of mechanical components. This direct transmission also lowers energy consumption during operation, leading to a more dexterous, compact, reliable, and cost-efficient design. Furthermore, one of the notable advantages of the proposed design is the ability to modify the manipulator's support, as shown in Figure 3a, to adapt it to various joints found in biological organisms, as illustrated in Figure 3b. The designed spherical platform, inspired by the structure of a spherical ball bearing, allows for the symmetrical addition of a spherical arm and support, enabling the transformation of the system into a parallel robotic manipulator. This configuration enhances the system's mechanical stability, precision, and adaptability to complex tasks. Redundant configurations in robotic manipulators are often crucial for enhancing flexibility, dexterity, and fault tolerance. In the case of the novel bio-inspired 3DOF SRM (Figure 3), this redundancy can be implemented through the symmetrical arrangement of the support and spherical arm, thereby improving the system's adaptability to various tasks and operational conditions. This innovative design not only enhances the system's reliability but also significantly improves its robustness and adaptability, making it well suited for applications in complex and dynamic environments where precision, fault tolerance, and versatility are paramount.

The proposed novel method, which involves the transformation of geometric entities, conceptualizes joints found in living organisms as CSKPs and analyzes their kinematic parameters as geometric entities. This approach simplifies the analytical process, enhancing its effectiveness. Furthermore, it significantly contributes to the design of robotic manipulators by ensuring improved efficiency and precision.

Degree of Freedom Calculations for the Novel Bio-Inspired 3DOF SRM

Determining the DOF in robotic manipulators is a fundamental process, as it provides a comprehensive understanding of the number of independent movements that the system can perform. This insight is critical for both the precise design and the accurate control of the robot's motion, ensuring that the manipulator operates with maximum efficiency and optimal performance. Understanding the DOF is essential for preventing self-collisions and avoiding interference with external objects, thus, contributing to the overall safety and reliability of the system. The DOF of the novel bio-inspired 3DOF SRM, depicted in Figures 2b and 3, can be calculated using the Euler and Kutzbach formulas [94,95], as shown in Equation (9) since the constraints imposed by the kinematic pairs are not entirely independent.

$$M = \lambda L + \sum_{i=1}^{j} f_i + q,\ L = l - j - 1 \tag{9}$$

where

j is the number of joints in the manipulator;

l is the number of links in the manipulator;

λ is the closed-loop motion parameter that describes the positions and orientations of the couple in the loop;

f_i is the DOF of kinematic pairs on the manipulator;

q is the number of independent coordinates required to describe the motion.

For the given expressions, we can calculate the complete count of constraints $\{d\}_0^5$ within the subspace of the end effector as follows (10):

$$d = 6 - \lambda \tag{10}$$

By inputting the values of l = 4, j = 4, λ = 3, $\sum_{i=1}^{j} f_i = 5$, and q = 1 into the novel 3DOF SRM shown in Figure 2b, we can determine its DOF to be M = 3. Since Figure 3a represents an open configuration, both configurations maintain a degree of freedom of $M = 3$.

In addition to defining movement capabilities, calculating the DOF optimizes mechanical design by preventing over or under constraining, improving energy efficiency, and reducing wear. It also aids in integrating control algorithms to enhance precision and responsiveness, ensuring the manipulator operates efficiently in dynamic environments.

4. Kinematic Analysis of the Novel Bio-Inspired 3DOF SRM

The introduction of the geometric entity transformation approach, which integrates both forward and inverse kinematics concepts, is significantly enhanced by the application of the screw theory. This methodology provides a cohesive and comprehensive framework for elucidating the intricate relationship between joint motions and end effector movements. Such a holistic perspective fosters a more intuitive understanding of the robot's behavior, thereby facilitating improved decision making regarding trajectory planning, obstacle avoidance, and overall system optimization.

The kinematic structure of the proposed manipulator is designed with two revolute pairs that drive concentric arcs, in addition to a third revolute pair located on a platform (Figure 4). In this specific isocenter configuration, the joints of the manipulator are arranged such that all perpendicular axes intersect at a common point. The centers of the arcs, designated as O_1 and O_2, are positioned at specific locations as illustrated in Figure 4.

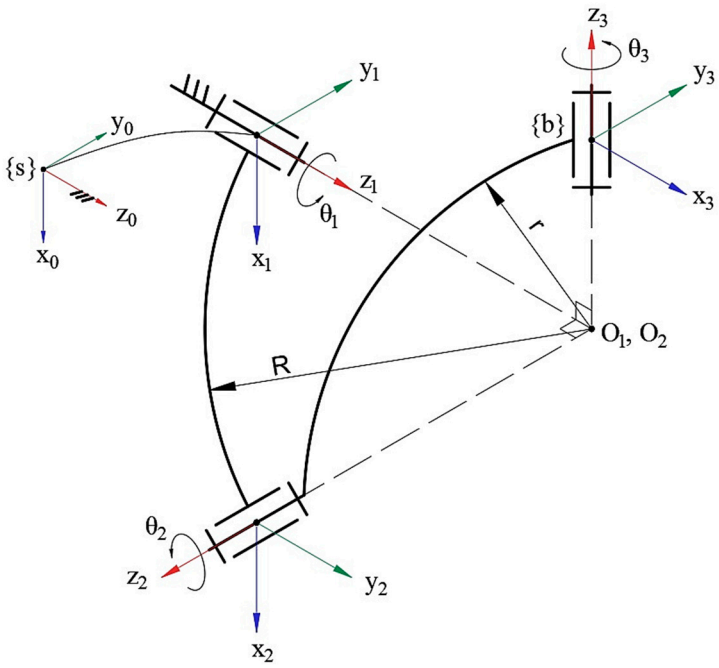

Figure 4. Kinematic structure of the proposed novel bio-inspired 3DOF SRM.

According to Chasles-Mozzi's theorem [96], it is a well-established principle that any rigid body displacement can be effectively represented as a motion along a fixed screw axis, S, within a three-dimensional space. Brockett [97] demonstrates that the forward kinematic equations of an open chain robot, comprising either revolute or prismatic joints, can consistently be expressed as a product of matrix exponentials. This underscores the significance of the product of the exponentials (PoE) formula as a valuable modeling tool in robot kinematics.

In the subsequent phase, the PoE representation is employed to determine both the position and orientation of the end effector, which is to be positioned on the mobile platform of the novel bio-inspired 3DOF SRM, using a forward kinematic approach. In our design, for the fixed frame $\{s\}$ and the end effector frame $\{b\}$ as illustrated in Figure 4, the forward kinematics in PoE formulation is represented as follows (11):

$$T(\theta) = e^{[S_1]\theta_1}\, e^{[S_2]\theta_2}\, e^{[S_3]\theta_3}\, M \tag{11}$$

The zero position configuration of the end effector, denoted as M, is defined by the following Equation (12):

$$M = \begin{bmatrix} 0 & 0 & -1 & -r \\ 0 & 1 & 0 & 0 \\ 1 & 0 & 0 & R \\ 0 & 0 & 0 & 1 \end{bmatrix} \tag{12}$$

The values of the screw parameters, $S_i = \omega_i,\ v_i$, are listed in the following Table 1:

Table 1. Screw parameters table for novel bio-inspired 3DOF SRM.

Frame$i$	ω_i	q_i	V_i=$-\omega_i \times q_i$
1	(0, 0, 1)	(0, 0, 0)	(0, 0, 0)
2	(0, −1, 0)	(0, 0, R)	(R, 0, 0)
3	(−1, 0, 0)	(−r, 0, 0)	(0, 0, 0)

The variables ω_i, q_i, and V_i represent the angular velocity, coordinate, and linear velocities, respectively, for each frame, i, of the zero position of the designed manipulator, as listed in Table 1.

The kinematic matrix, $T(\theta)$, which represents the orientation and position of the selected point $\{b\}$ on the z rotation axis of the novel bio-inspired 3DOF SRM, relative to the fixed frame $\{s\}$ at any given moment, is defined as follows (13):

$$T(\theta) = \begin{bmatrix} -c_1s_2c_3 - s_1s_3 & c_1s_2s_3 - s_1c_3 & -c_1c_2 & Rc_1s_2 - rc_1c_2 - R(s_1s_3 + c_1c_3s_2) \\ -s_1s_2c_3 + c_1s_3 & s_1s_2s_3 + c_1c_3 & -s_1c_2 & R(c_1s_3 - c_3s_1s_2) - rc_2s_1 + Rs_1s_2 \\ c_2c_3 & -c_2s_3 & -s_2 & Rc_2c_3 - R(c_2 - 1) - rs_2 \\ 0 & 0 & 0 & 1 \end{bmatrix} \quad (13)$$

where the variables c_1, c_2, c_3, and s_1, s_2, s_3 in the matrix (13), represent the trigonometric functions, cosine and sine, of angles θ_1, θ_2, and θ_3 respectively.

The Jacobian $J_s(\theta)$, which establishes the relationship between the angular velocity of the end effector and the linear velocity of the joints of the designed novel bio-inspired 3DOF SRM, is determined by the following Formula (14):

$$J_s(\theta) = \begin{bmatrix} \omega_{S1} & \omega_{S2} & \omega_{S3} \\ V_{S1} & V_{S2} & V_{S3} \end{bmatrix} = \begin{bmatrix} 0 & \sin(\theta_1) & -\cos(\theta_1)\cos(\theta_2) \\ 0 & -\cos(\theta_1) & -\cos(\theta_2)\sin(\theta_1) \\ 1 & 0 & -\sin(\theta_2) \\ 0 & R\cos(\theta_1) & 0 \\ 0 & R\sin(\theta_1) & -r\sin(\theta_2) \\ 0 & 0 & r\cos(\theta_2)\sin(\theta_1) \end{bmatrix} \quad (14)$$

The post-rotation angular and linear velocities for each joint of the novel 3DOF SRM can be expressed as follows: $\omega_{S1} = [0, 0, 1]'$, $\omega_{S2} = [\sin(\theta_1), -\cos(\theta_1), 0]'$, $\omega_{S3} = [-\cos(\theta_1)\cos(\theta_2), -\cos(\theta_2)\sin(\theta_1), -\sin(\theta_2)]'$ and $V_{S1} = [0, 0, 0]'$, $V_{S2} = [R\cos(\theta_1), R\sin(\theta_1), 0]'$, $V_{S3} = [0, -r\sin(\theta_2), r\cos(\theta_2)\sin(\theta_1)]'$.

The spatial velocity or twist of the end effector of the novel bio-inspired 3DOF SRM can be calculated by utilizing the Formula (15) and taking into account the given velocities ($\dot{\theta} = \left[\dot{\theta_1}, \dot{\theta_2}, \dot{\theta_3}\right]'$) as follows:

$$V_{twist} = J_s(\theta)\,\dot{\theta} \quad (15)$$

Inverse Kinematic Analysis of the Novel Bio-Inspired 3DOF SRM

Inverse kinematics is a fundamental aspect of robotic manipulators as it allows for the determination of joint angles and positions required to achieve a desired end effector configuration ($T(\theta)$). This capability is essential for controlling the movement and positioning of robotic arms in various applications such as industrial robotics, medical robotics, mobile robotics, animation, virtual reality, and computer graphics. When it comes to achieving inverse kinematics, there are several approaches available, including analytical solutions, closed-form solutions, numerical optimization methods, geometric methods, and machine learning-based techniques.

Numerical optimization methods play a crucial role in the inverse kinematics of robotic manipulators, as they provide an advantageous approach for solving complex mathematical equations and constraints, allowing for accurate and efficient determination of joint angles and positions, leading to improved robot control, motion planning, and task execution. These methods allow for a more flexible and adaptable approach to problem-solving, enabling researchers to tackle intricate scenarios that would otherwise be challenging or impossible to solve analytically. Even if an analytic solution is theoretically possible, it is

often advantageous to employ numerical optimization methods to improve the accuracy of the results.

In this study, the implementation of the inverse kinematics problem for a novel bio-inspired 3DOF SRM is carried out by utilizing the Levenberg–Marquardt numerical optimization algorithm [98,99]. The Levenberg–Marquardt algorithm is a numerical optimization method that combines the strengths of the Gauss–Newton algorithm and the method of gradient descent. It is designed to solve nonlinear least squares problems, where the goal is to find the parameters that minimize the sum of squared differences between observed and predicted values. In comparison to the Gauss–Newton algorithm, the Levenberg–Marquardt algorithm demonstrates greater robustness, enabling it to converge towards a solution even when the initial guess is far from the desired minimum.

To gain a comprehensive understanding of the mathematical expressions underlying the Levenberg–Marquardt algorithm, it is essential to delve into the intricacies of a general nonlinear least squares problem. We have a set of m data points (x_i, y_i) and a model function $f(x, p)$, where x is the independent variable and p represents the vector of parameters to be optimized. The goal is to find the optimal parameter vector, $p^* = \left[\theta_1', \theta_2', \theta_3'\right]^{\mathrm{T}}$, that minimizes the sum of squared residuals (S) (16):

$$S(p) = \sum_{i=1}^{m} [y_i - f(x, p)]^2 \tag{16}$$

The Levenberg–Marquardt algorithm operates by iteratively updating a parameter vector, denoted as p, until convergence is achieved. Each iteration involves computing a search direction, represented as Δp, which indicates how much each parameter should be updated. The update rule (p_{new}) can be expressed as follows (17):

$$p_{new} = p_{old} + \Delta p \tag{17}$$

The search direction, Δp, is obtained by solving a linear system of equations, which involves the Jacobian matrix, J, and the residual vector, r_{res}. The Jacobian matrix, J, is defined as (18):

$$J_{ij} = \frac{\partial f(x_i, p)}{\partial p_j} \tag{18}$$

where $\frac{\partial f(x_i, p)}{\partial p_j}$ denotes the partial derivative of f with respect to the j-th parameter. The residual vector, r_{res}, is defined as follows (19):

$$r_{res_i} = y_i - f(x_i, p) \tag{19}$$

To solve the linear system of equations, the Levenberg–Marquardt algorithm introduces a damping factor, λ, that controls the trade-off between the Gauss–Newton method (which assumes a locally linear model) and gradient descent (which assumes a locally quadratic model). The update rule for Δp can be written as (20):

$$\left(J^T J + \lambda I \right) \Delta p = J^T r_{res} \tag{20}$$

In this expression, J^T denotes the transpose of the Jacobian matrix, I is the identity matrix, and λI is added to ensure the system is well conditioned.

The damping factor, λ, is adjusted at each iteration based on the improvement in the objective function. If the new parameter vector, p_{new}, leads to a decrease in the objective function, λ is decreased to favor the Gauss–Newton method. Conversely, if the objective function increases, λ is increased to favor gradient descent. This adaptive adjustment of

λ allows the algorithm to efficiently navigate through parameter space and converge to a local minimum.

The successful solution of the inverse kinematics for the developed novel bio-inspired 3DOF SRM is achieved by implementing the Levenberg–Marquardt numerical optimization algorithm in the MATLAB program and utilizing the $T(\theta)$ transformation matrix (13), leading to the determination of the angles $[\theta'_1, \theta'_2, \theta'_3]$. The angles θ'_1, θ'_2, and θ'_3 required to determine the new position of the end effector of the robotic manipulator in space can be effortlessly derived by utilizing the expressions of the observed and expected transformation matrices [100] provided below (21):

$$e^{[S_1]\theta'_1} e^{[S_2]\theta'_2} e^{[S_3]\theta'_3} = e^{[S_1]\theta_1} e^{[S_2]\theta_2} e^{[S_3]\theta_3} M \tag{21}$$

where the observed transformation matrix on the right-hand side of expression (21) can be determined by utilizing Expression (13), while the expected transformation matrix is on the left-hand side.

The Levenberg–Marquardt algorithm is implemented using the "*lsqnonlin*" function in the MATLAB environment. The objective function, called "*calculateResiduals*", is responsible for computing the residuals between the observed and expected transformation matrices (21) based on the current parameter values. Through an iterative process, the algorithm adjusts these parameters to minimize the residuals. Upon completion of the optimization process, the resulting values of $\hat{\theta}_1$, $\hat{\theta}_2$, and $\hat{\theta}_3$ are extracted from the optimization result.

The Levenberg–Marquardt algorithm continues iterating until a stopping criterion is met, such as reaching a maximum number of iterations or achieving a desired level of convergence. The final parameter vector, $p^* = \left[\theta'_1, \theta'_2, \theta'_3\right]^{\mathrm{T}}$, obtained represents the optimal solution to the nonlinear least squares problem.

Combining inverse kinematics with optimization methods is essential for accurately determining the structural parameters of the novel bio-inspired 3DOF SRM and achieving precise control over its operation (Figure 12).

5. Experimental Validation and Performance Results of the Novel Bio-Inspired 3DOF SRM

This experimental study aims to rigorously assess the performance of the novel bio-inspired 3DOF SRM, designed as an application of the wrist joint observed in humans (Figure 1). A straightforward control methodology has been developed to compute the target angles (roll (α), pitch (β), and yaw (γ)) required for the rotation of the manipulator's mobile platform. The inverse kinematic calculations leverage the specified target orientation to derive the necessary rotational angles for the three motors, thereby facilitating precise control of the manipulator's movements. Following the theoretical analysis, the dynamic modeling of the system is conducted within the MATLAB environment to facilitate usability. Once the updated 3D CAD model is developed with the appropriate assembly constraints, it is imported into the SimMechanics module of MATLAB for trajectory planning purposes, as illustrated in Figure 5a and further visualized in the 3D representation in Figure 5b.

In the analyzed system, the input signals and their associated constraints are formulated as MATLAB functions, providing a structured and systematic framework to analyze the interconnections among control system components (Figure 5). This approach facilitates a detailed examination of the sequential interactions between system elements and the identification of critical parameters for precise measurement, thereby enhancing the comprehensiveness and clarity of the control system analysis.

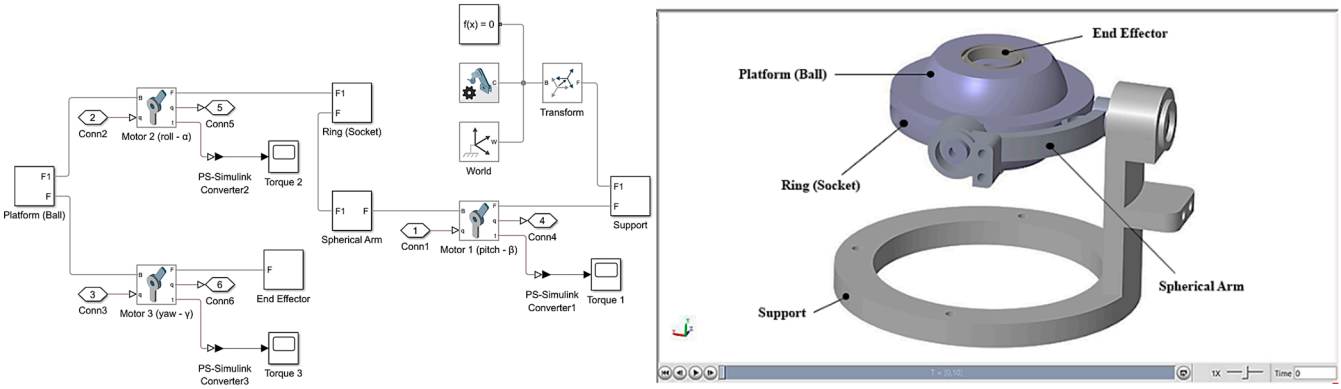

(**a**) (**b**)

Figure 5. Implementation of the novel bio-inspired 3DOF SRM in the MATLAB SimMechanics environment: (**a**) Control system block diagram; (**b**) 3D model highlighting key components, including the end effector, spherical arm, ring (socket), platform (ball), and support.

Following the theoretical design and simulation phases, the components of the manipulator are fabricated using a Dremel 3D45 Idea Builder 3D printer and subsequently assembled with the aid of three servo motors, as illustrated in Figure 6a. A Teensy 4.0 microcontroller is employed to facilitate connectivity among the various components. The system is powered by a lithium polymer (LiPo) battery, which provides a nominal voltage of 12 volts. This voltage is then regulated to five volts for the microcontroller, encoders, and logic signal levels, while the unregulated voltage is transmitted directly to the controlling motors.

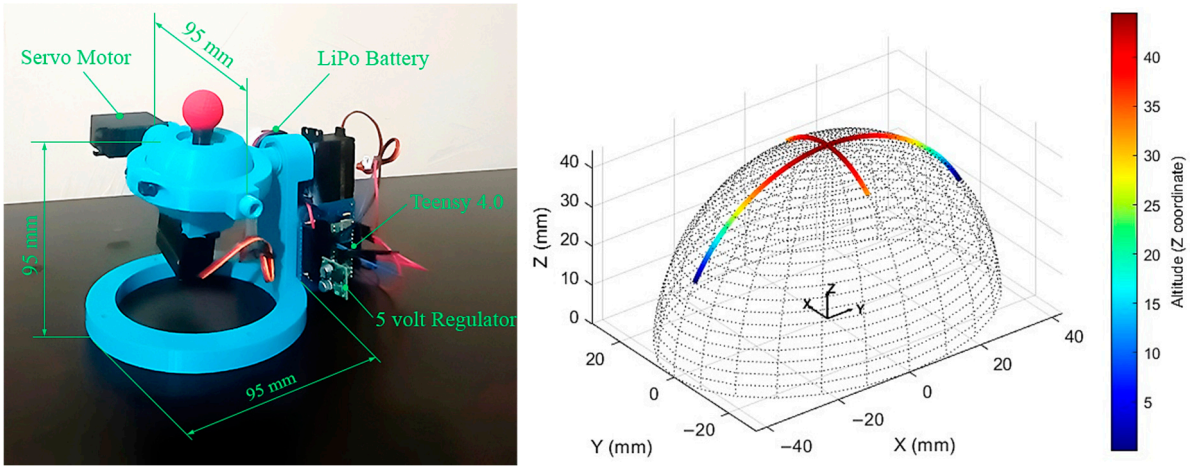

(**a**) (**b**)

Figure 6. (**a**) Configuration and dimensions of the novel bio-inspired 3DOF SRM. (**b**) Workspace representation of the end effector's motion trajectory in the novel bio-inspired 3DOF SRM.

The motion trajectory of the end effector, represented by the reflector indicated by the red sphere in Figure 6a, is analyzed using Python, employing the OpenCV library for object tracking and NumPy for numerical computations. Additionally, MATLAB is integrated into the analysis, and the resulting workspace of the manipulator is illustrated in Figure 6b, demonstrating its operational range along with the corresponding angles.

5.1. Lagrangian Dynamics and Analytical Discussions of the Novel Bio-Inspired 3DOF SRM

The dynamics of the novel bio-inspired 3DOF SRM are theoretically analyzed using the Lagrangian method, based on the homogeneous transformation matrix, $T(\theta)$, as presented in Equation (13), to validate the results obtained from the MATLAB Simulink simulations.

The Lagrangian, $\mathcal{L}\left(\underline{q}, \underline{\dot{q}}\right)$, defined as the difference between the system's total kinetic energy, $K\left(\underline{q}, \underline{\dot{q}}\right)$, and potential energy, $P\left(\underline{q}, \underline{\dot{q}}\right)$, is formulated as (22):

$$\mathcal{L}\left(\underline{q}, \underline{\dot{q}}\right) = K\left(\underline{q}, \underline{\dot{q}}\right) - P\left(\underline{q}\right) \tag{22}$$

In this context, $\underline{q} = [\theta_1, \theta_2, \theta_3]$ denotes the generalized joint angles, and $\underline{\dot{q}} = \left[\dot{\theta_1}, \dot{\theta_2}, \dot{\theta_3}\right]$ denotes their corresponding generalized angular velocities. The designed robotic manipulator, modeled as a rigid body, has its kinetic energy expressed as follows (23):

$$K\left(\underline{q}, \underline{\dot{q}}\right) = \frac{1}{2}\sum_{i=1}^{n}\sum_{j=1}^{n} m_{ij}(\underline{q})\underline{\dot{q}}_i\underline{\dot{q}}_j = \frac{1}{2}\underline{\dot{q}}^T M_s(\underline{q})\underline{\dot{q}} \tag{23}$$

Here, $m_{ij}(\underline{q})$ represents the (i, j) -th element of the nxn mass matrix, $M_s(\underline{q})$. The mass matrix, $M_s(\underline{q})$, is defined as follows (24):

$$M_s\left(\underline{q}\right) = \sum_{i=1}^{n}\left(m_i\, J_{v_i}^T + J_{\omega_i}^T\, I_i\, J_{\omega_i}\right) \tag{24}$$

In this expression, J_{vi} is the Jacobian matrix associated with the linear velocity, $J_{\omega i}$ is the Jacobian matrix for angular velocity, I_i denotes the inertia tensor of the i-th link relative to its center of mass, and m_i is the mass of the i-th link. The potential energy of the robotic system is determined using the following Equation (25):

$$P\left(\underline{q}\right) = \sum_{i=1}^{n} m_i g h_i \tag{25}$$

Here, g denotes the gravitational acceleration, and h_i is the height of the i-th link's center of mass. The equations of motion [100] are derived from the Lagrangian using the Euler–Lagrange Equation (26):

$$F_i = \frac{d}{dt}\left(\frac{\partial \mathcal{L}}{\partial \underline{\dot{q}_i}}\right) - \frac{\partial \mathcal{L}}{\partial \underline{q_i}} + \sum_{j=1}^{p}\lambda_j a_{ji},\ i = 1, = \ldots, n \tag{26}$$

where F_i denotes the generalized external forces acting on the system, such as torques or external loads, while $\lambda_j a_{ji}$ are the generalized constrint forces. The angles $\theta_1, \theta_2, \theta_3$ correspond to the roll (α), pitch (β), and yaw (γ) motor angles of the manipulator, respectively. This analysis considers only internal forces, accounting for gravitational forces but excluding external and frictional forces from the system. The motor torque data are determined using the inertia tensor information obtained from the CAD model of the designed robotic manipulator, which is created with identical proportions (see Figure 6a). The resulting torque values for the motors are presented in Figure 7b. Consequently, the Euler–Lagrange equation simplifies to $F_i = 0$.

During the analysis, MATLAB's symbolic toolbox is employed to implement constraints on the motor angles to avoid collisions between mechanical components. These constraints around the initial position, set at 90 degrees, are specified as $30^\circ \leq \beta \leq 150^\circ$, $60^\circ \leq \alpha \leq 120^\circ$, $0^\circ \leq \gamma \leq 180^\circ$. In the following sections, the dynamic behavior of the robotic manipulator will be examined by evaluating the torque values of the motors and applying external loads to its end effector (Figures 8 and 9).

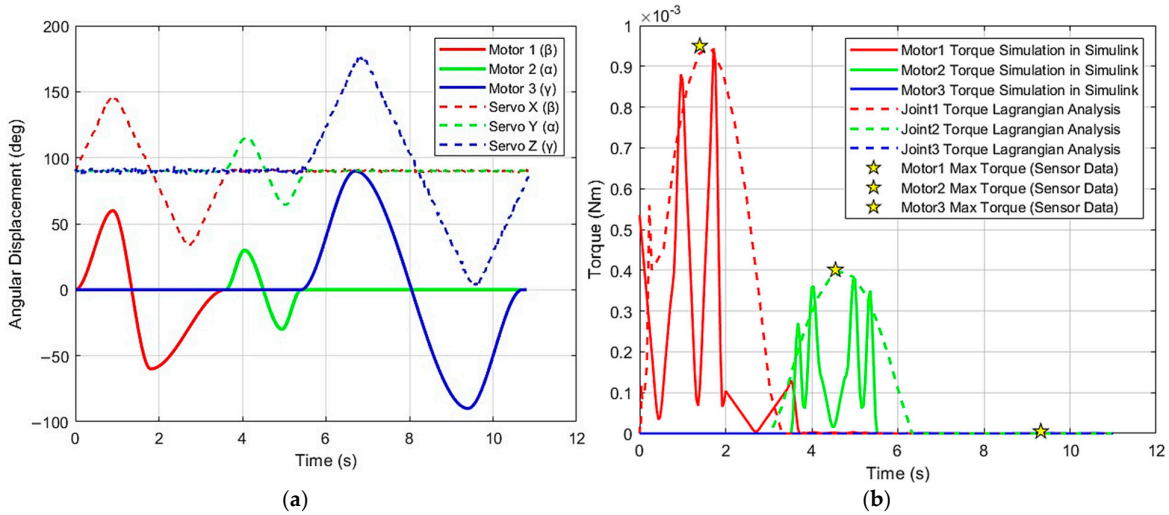

(**a**) (**b**)

Figure 7. (**a**) Comparative analysis of simulation and experimental plots depicting the angular displacement profiles of the motors for the novel bio-inspired 3DOF SRM. (**b**) Torque profiles of the motors for the novel bio-inspired 3DOF SRM.

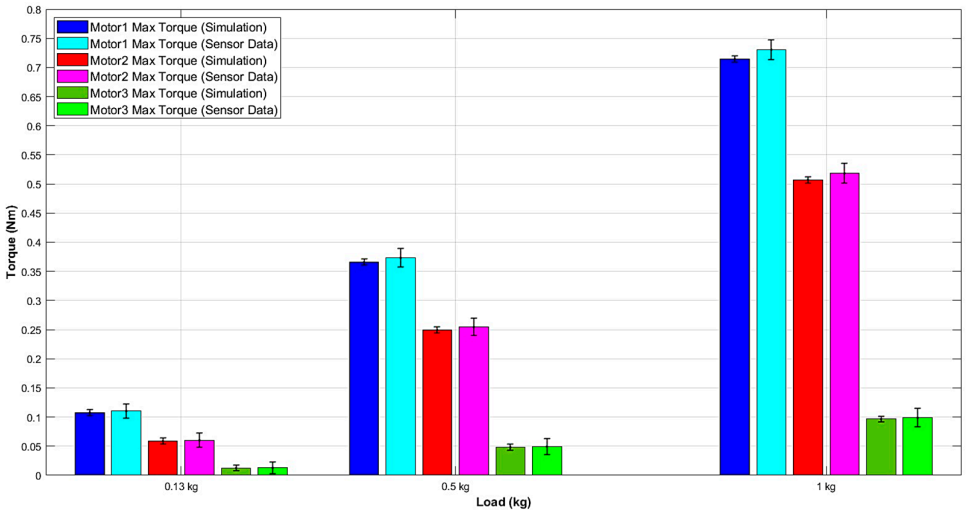

Figure 8. Torque performance evaluation of the novel bio-inspired 3DOF SRM under variable load conditions. Error bars represent the standard error of simulation values, and the deviation was measured using the ACHS-7124 Current Sensor Carrier.

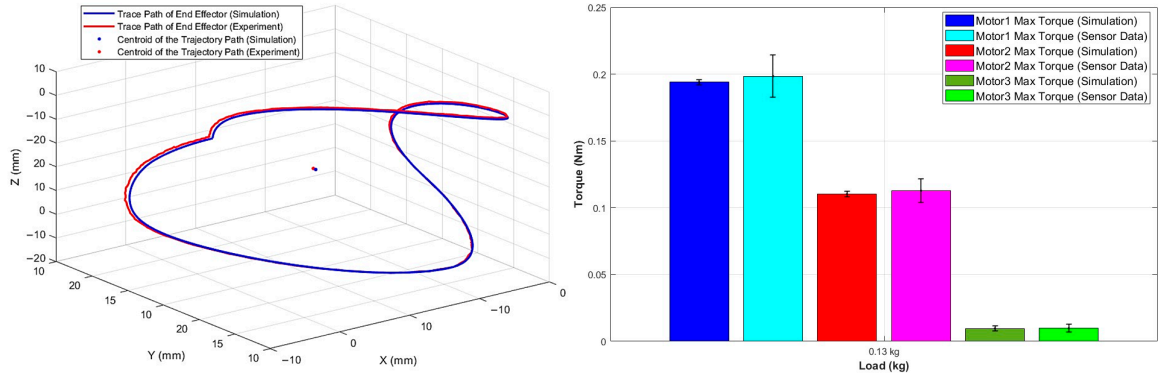

(**a**) (**b**)

Figure 9. (**a**) Comparative analysis of the complex trajectory paths of the novel bio-inspired 3DOF SRM's end effector, as obtained from simulation and experimental tests. (**b**) Cross-analysis of the dynamic behavior of the motors during the execution of the complex trajectory. Error bars represent the standard errors for both simulation and experimental data.

To analyze the kinematic and dynamic properties of the examined manipulator, performance measurements are conducted over a 12 s interval, incorporating both simulation and experimental results, as shown in Figure 7. The solid lines represent the outcomes of the simulation for Motor 1, Motor 2, and Motor 3, while the dashed lines illustrate the roll (α), pitch (β), and yaw (γ) angles for Servo X, Servo Y, and Servo Z, as obtained from the experimental data (Figure 7a).

The investigation revealed that the maximum range of motion is ± 30 degrees along the roll (α) axis, ± 60 degrees along the pitch (β) axis, and ± 180 degrees along the yaw (γ) axis. Notably, the difference between the simulation and experimental results is found to be less than ± 1 degree, indicating a high level of accuracy in the designed model.

Figure 7b presents the comparative torque profiles obtained from MATLAB Simulink and Lagrangian dynamics for the three motors in the manipulator design. Motor 1 exhibits significant torque fluctuations, peaking at approximately 9.5×10^{-4} Nm during initial operation, indicating a high torque demand during movement initiation. In contrast, Motor 2 maintains lower and more stable torque values, peaking at 4.6×10^{-4} Nm, with a brief peak followed by a rapid decline, suggesting a relatively consistent torque requirement. We observe that Motor 3 shows no torque output throughout the duration due to the absence of weight along the z-axis, indicating that this motor does not encounter significant loading under the tested conditions. The maximum torque values for each motor, obtained experimentally via current measurements using the ACHS-7124 Current Sensor Carrier (manufactured by Pololu Corporation, Las Vegas, Nevada, USA) and MG996R Metal Gear (manufactured by Miuzei Company, Shenzhen, China) servo motors, are marked by star symbols. The comparison between the MATLAB simulation, Lagrangian dynamics, and current sensor data reveal a minor deviation, with a percentage error of approximately 0.21%, demonstrating the accuracy and consistency between the different methods used for torque analysis.

In the subsequent phase of the research, a comparative analysis of torque values is performed by applying varying load conditions to the end effector of the robotic manipulator (Figure 8). This analysis is crucial for evaluating the system's mechanical stability, dynamic response, torque distribution, speed, and precision. Testing the robotic manipulator under diverse operating conditions provides valuable insights into its practical functionality and overall performance.

Figure 8 presents a comparative analysis of the maximum torque outputs for the three motors (Motor 1, Motor 2, and Motor 3) subjected to three distinct load values (0.13 kg, 0.54 kg, 1.0 kg). Torque data are acquired through simulations and experimental measurements using sensors to assess the manipulator's consistency and accuracy. A $22lb/0.04oz$ Precision Digital Scale is employed to precisely determine the mass of each load during the study.

The error bars in Figure 8 reflect the combined effect of simulation errors ($\pm 0.5\%$ standard error) and experimental deviations ($\pm 1.5\%$ standard deviation from the ACHS-7124 Current Sensor Carrier) used in the analysis of the motors' maximum torque outputs.

In the initial phase of the research, a novel bio-inspired 3DOF SRM is integrated with a robotic hand mechanism (Figure 12a) and tested under various load conditions. This phase accounted for gravitational and frictional forces within the kinematic pairs. The maximum torque value, 0.11 Nm, derived from simulations and experimental tests, exhibited a minimal error margin of 0.8%, reflecting the manipulator's precise functionality.

In the second phase, applying a 0.5 kg load, the system recorded a maximum torque of 0.37 Nm, with an error of 0.5%. During the final phase, under a 1 kg load, the torque output peaked at 0.73 Nm, with an estimated error of 0.7%.

Across all stages, the experimental results demonstrated less than a 1% deviation from simulation predictions, highlighting the robotic manipulator's exceptional precision and seamless performance.

To assess the adaptability of the designed robotic manipulator under various test conditions, it is programmed to follow a complex trajectory that facilitates the movement of a red sphere placed on a mobile platform (see Figure 6a). The trajectory of the red sphere is recorded and visualized in Figure 9a. Although the end effector's trajectory path, determined through simulations and mathematical calculations (as shown in Equation (13)), exhibited high consistency, some deviations are observed during experimental tests. Numerical data extracted from the CSV files during both the simulation and experimental phases revealed a root mean square (RMS) error of 0.192 mm. Additionally, the difference between the centroids of the trajectory paths is calculated to be 0.143 mm, underscoring the manipulator's precision and accuracy in real-world applications.

To evaluate the dynamic behavior illustrated in Figure 9b of the novel bio-inspired 3DOF SRM, its movement along a complex trajectory (Figure 9a) is analyzed with an attached robotic hand by comparing the motor performance in simulations and experiments. The maximum torque values recorded are 0.198 Nm for Motor 1, 0.112 Nm for Motor 2, and 0.009 Nm for Motor 3. The maximum error is approximately 0.8%, demonstrating the robotic system's high precision and stable and reliable performance under dynamic conditions.

This analysis offers valuable insights into the operational limits and capabilities of the manipulator, paving the way for further advancements in robotic design and control strategies.

5.2. Adaptability of the Novel Bio-Inspired 3DOF SRM in Biomimetic Applications

Utilizing bio-inspired principles enables the novel bio-inspired 3DOF SRM to emulate the functionality of 3DOF joints observed in various living organisms, offering a compelling alternative to traditional engineering approaches [45–55]. In this section, we evaluated the adaptability of the designed robotic manipulator by simulating its operation as a shoulder joint in the human arm (Figure 10). The mass of the novel bio-inspired 3DOF SRM is measured at 0.300 kg, while the attached robotic arm weighed 0.450 kg. As illustrated in Figure 10, the novel bio-inspired 3DOF SRM demonstrated sufficient effectiveness to enable the robotic arm to reach any desired position in space, showcasing its versatility and adaptability for a range of applications.

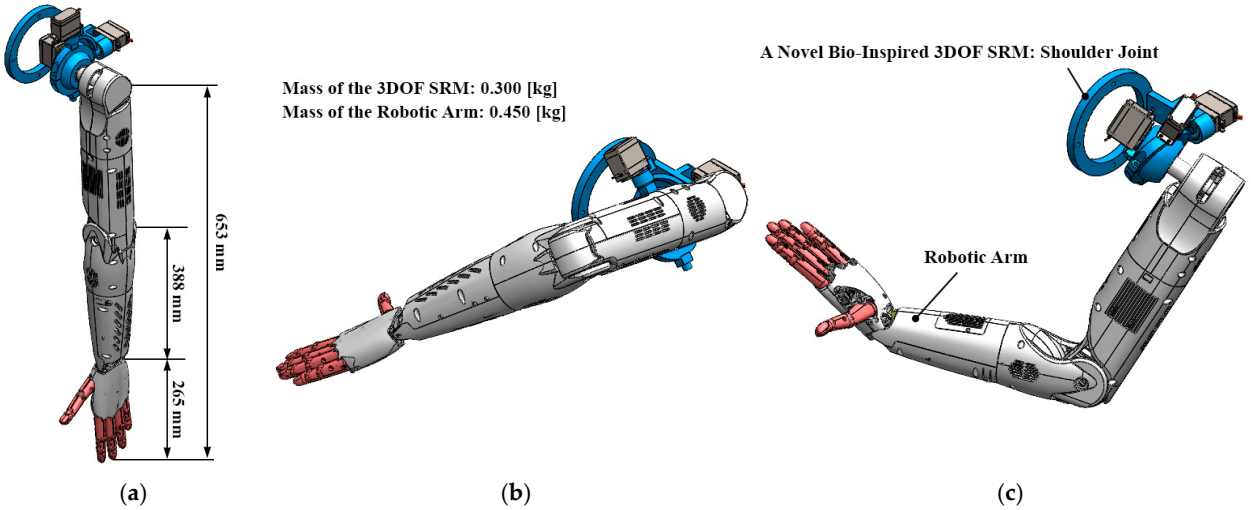

Figure 10. Illustration of the novel bio-inspired 3DOF SRM functioning as a shoulder joint. (**a**) Initial position with linear dimensions of the robotic arm. (**b**) The second position displays the mass values of the robotic system. (**c**) The third position illustrates the versatility and adaptability of the robotic system.

In Figure 10, the designed system is tested with a complex trajectory during simulation to evaluate its kinematic parameters. The simulation results for the pitch (β), roll (α), and yaw (γ) angles, corresponding to Motor 1, Motor 2, and Motor 3, respectively, are plotted as functions of time in Figure 11a.

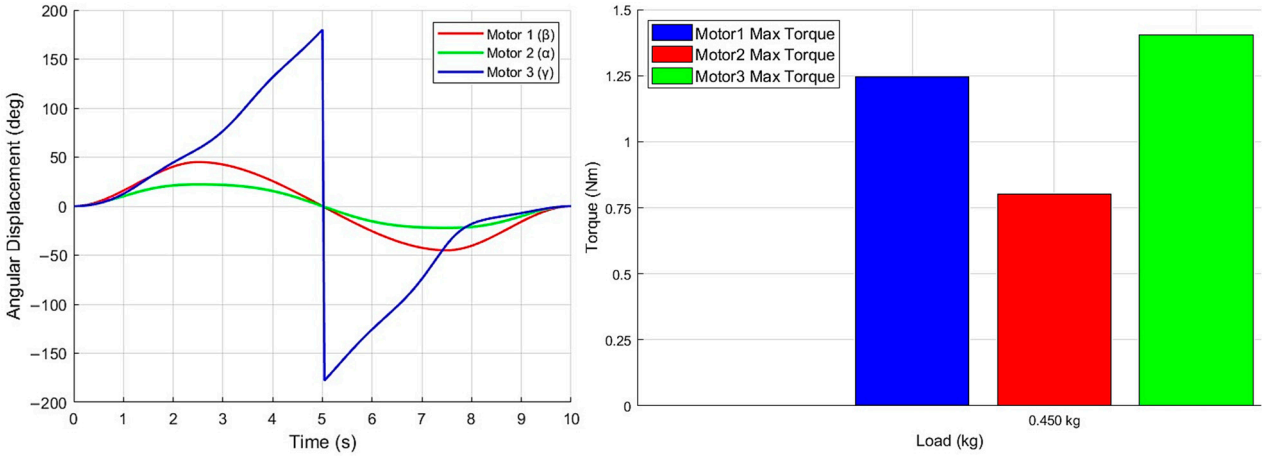

(**a**) (**b**)

Figure 11. Simulation results for the novel bio-inspired 3DOF SRM applied as a shoulder joint in a robotic arm. (**a**) Time-dependent angular displacement graph for the motor angles (roll, pitch, and yaw) of the 3DOF SRM. (**b**) Torque values of the motors during the execution of a complex trajectory motion by the 3DOF SRM.

During the simulation, the highest maximum torque value recorded is 1.4 *Nm* (Figure 11b), indicating that the system achieves the required performance with minimal motor power consumption, underscoring its efficiency.

This section highlights the application of the novel bio-inspired 3DOF SRM as a shoulder joint, emphasizing its adaptability across various systems [9–27]. This versatility suggests a wide range of potential applications [75–87] for the robotic manipulator. The designed manipulator is well suited for replicating 3DOF joints observed in living organisms, making it a promising candidate for future robotic system designs. Consequently, the manipulator is proposed as a practical and efficient option for researchers in advancing robotic applications.

5.3. Human–Robot Interaction Through the Novel Bio-Inspired 3DOF SRM

In the subsequent phase of the research, the novel bio-inspired 3DOF SRM is utilized as a model for the 3DOF wrist mechanism observed in humans, as illustrated in Figure 12a. This study introduces an innovative control system for a bio-inspired 3DOF wrist robotic manipulator that utilizes real-time hand tracking to facilitate intuitive and adaptive manipulation. As previously discussed, the development of robotic systems that can interact seamlessly with human users represents a critical advancement in the field of robotics (Figure 1).

Figure 12a depicts the book as the target object for retrieval, facilitated by establishing a connection between the mini wireless surveillance camera system and the 3DOF wrist manipulator. The control system is engineered to leverage hand-tracking data to compute the requisite angles for the servo motors that govern the manipulator's movements, utilizing real-time data sourced from the Arduino interface. Specifically, the positions of the 3DOF wrist and finger joints are extracted through MediaPipe, allowing for the computation of a centroid that represents the palm's position, as defined by a proximity sensor. This centroid is pivotal in adjusting the end effector's position, enabling precise control for object detection within the operational capabilities of the robotic manipulator. The integration of Python with the OpenCV and MediaPipe libraries facilitates accurate gesture

recognition and effective tracking of hand landmarks, thereby significantly enhancing the manipulator's responsiveness to user inputs (Figure 12b).

(**a**) (**b**)

Figure 12. (**a**) Coordination framework of the novel bio-inspired 3DOF SRM for human–robot interaction. (**b**) Real-time hand tracking, object detection, and servo angle measurements for the bio-inspired 3DOF SRM.

During human–robot interaction, the acquisition of objects is facilitated by an E18-D80NK proximity sensor that displays the message "Object Detected" on the screen when the robotic hand detects an object, aiding in tracking and guiding the manipulator's approach.

The presented control system represents a significant advancement in the development of intelligent robotic manipulators capable of real-time interaction. Future research will concentrate on optimizing gesture recognition algorithms and expanding the range of manipulative tasks, thereby enhancing the practical applications of bio-inspired robotic systems.

The bio-inspired novel 3DOF SRM developed in this study has significant potential for various applications, including military, industrial, and medical fields. Its advanced control system and intuitive human–robot interaction capabilities enhance precision and efficiency in tasks such as bomb disposal, automated assembly, and minimally invasive surgeries. Furthermore, our proposed human–robot interaction system eliminates the need for specially designed gloves to control the manipulator, as the user-friendly interface accommodates any hand size by tracing its components. In comparison to other teleoperation systems [101–105], the novel bio-inspired 3DOF SRM offers cross-platform compatibility, a mobile base, lower costs, an expanded workspace, and a more efficient end effector. This adaptability facilitates integration with advanced technologies, such as virtual reality headsets (e.g., Oculus Rift and HTC Vive) and augmented reality glasses (e.g., Microsoft HoloLens and Google Glass), enabling intuitive control and enhancing user experience. Besides this, our system supports various input devices, including motion capture sensors (e.g., Leap Motion and Microsoft Kinect) and wearable technologies (e.g., smart rings and smart bracelets), which provide supplementary feedback and enhance interaction. As technology continues to evolve, this manipulator could play a pivotal role in addressing complex challenges across multiple sectors.

6. Conclusions and Future Work

In this research, we investigated biological organisms exhibiting 3DOF joint configuration and explored innovative robotic designs, culminating in the development of a bio-inspired novel 3DOF SRM. The design is performed by the transformation of CSKPs to effectively replicate the movements of ball and socket joints observed in biological organisms. This process highlights methodological efficiency in deriving the manipulator's kinematic parameters using geometrical objects. Throughout this process, we established three foundational axioms for the design and analysis of novel bio-inspired manipulators.

Employing the screw theory and the Levenberg–Marquardt algorithm, we successfully addressed the forward and inverse kinematics challenges associated with the manipulator.

Our research utilized SolidWorks (Version 2023), MATLAB (R2024a), Python (3.12), and Arduino IDE (Version 2.3.2) software for comprehensive design and comparative analysis of the manipulator. We presented extensive results detailing the spherical workspace of the novel bio-inspired 3DOF SRM, achieving roll $(\alpha) = \pm 30$ degrees, pitch $(\beta) = \pm 60$ degrees, and yaw $(\gamma) = \pm 180$ degrees. Additionally, a peak torque value of 9.5×10^{-4} Nm is measured under no-load conditions, highlighting the manipulator's lightweight design, high dexterity, and compact dimensions of 95 mm in height, width, and length.

In the next phase, the dynamic performance of the robotic manipulator is evaluated by applying three different loads (0.13 kg, 0.5 kg, and 1 kg) to its end effector. The highest recorded torque value is 0.73 Nm, with a maximum deviation of 0.8%. For the 0.13 kg load, a complex trajectory path was assigned to the novel bio-inspired 3DOF SRM to analyze its kinematic and dynamic performance. The RMS error is measured as 0.192 mm, while the difference between the centroids of the trajectory paths is calculated at 0.143 mm. During this motion, the maximum motor torque recorded is 0.198 Nm.

To further evaluate the adaptability of the designed 3DOF SRM, it was integrated with a robotic arm and tested through simulations for its kinematic and dynamic performance. In this phase, the maximum motor torque reached 1.4 Nm, demonstrating its capability to handle dynamic conditions effectively.

In the subsequent phase of this research, we implemented advanced methodologies and developed a user-friendly interface to enhance human–robot interaction. The novel bio-inspired 3DOF SRM is utilized as a model for the 3DOF wrist mechanism observed in humans, facilitating a more reliable hand–eye coordination process through the incorporation of a proximity sensor and a camera.

6.1. Design Innovations

Ball and socket joints observed in biological organisms exhibit an optimal and efficient design, serving as an inspiration for developing a bio-inspired novel 3DOF SRM in this study. The resulting design demonstrates a superior working zone compared to existing robotic manipulators [28–69] while maintaining a compact structure, enhanced flexibility, and energy efficiency. Furthermore, the manipulator integrates a mobile platform as its end effector, facilitating seamless attachment of additional components.

The design methodology encompassed the development of both constrained (Figure 2b) and fully independent configurations (Figure 3a) of the robotic manipulator. In both configurations, motion is transmitted directly from the motors to the platform without auxiliary mechanical components, minimizing mechanical losses due to friction and simplifying the overall design. In the constrained configuration (Figure 2b), the sequential motion is preserved, with the supporting structure absorbing additional loads to protect the motor from excessive torque. This feature renders the system particularly suitable for high-torque applications, such as robotic leg mechanisms, rocket maneuvering systems, and underwater robotic platforms.

The final iteration, a bio-inspired novel 3DOF SRM (Figure 3a), is an open-configured spatial manipulator. This design can be symmetrically adapted by incorporating supports and spherical arms, transforming it into a parallel-configured robotic manipulator and thereby broadening its functional scope. Parallel configurations are particularly advantageous in applications requiring enhanced flexibility, dexterity, and fault tolerance. Additionally, the modularity of the support structure allows for customization, enabling straightforward application in various domains where 3DOF configurations are required (Figure 3b).

6.2. Prospective Applications

Future research will focus on refining the 3DOF SRM platform for enhanced compactness and incorporating haptic feedback to improve control precision. While Figure 12 illustrates the teleoperation process within the scope of human–robot interaction, the proposed system offers substantial versatility and applicability across military, industrial, and medical domains.

Integrating the teleoperation system with the proposed manipulator offers substantial potential for industrial applications, particularly in operations involving remote positioning, transferring, and handling of manufactured components. These capabilities can substantially reduce production time and energy inefficiencies associated with material transport. Additionally, the aerospace and defense sectors represent promising avenues for implementation, particularly in high-risk or hazardous environments where remote operations can significantly enhance safety and operational efficiency. Such applications underscore the system's relevance in addressing challenges associated with complex operational scenarios.

In the medical domain, the flexibility and precision offered by the 3DOF manipulator and teleoperation technology hold transformative potential for minimally invasive surgeries, rehabilitation devices, and the precise manipulation of medical instruments. The system's compact and adaptive design makes it especially well-suited for applications requiring enhanced surgical accuracy and operational reliability.

In the subsequent stages of our research, we aim to investigate the application of this manipulator and system in terrestrial, aquatic, and aerial robotic systems, as well as in medical, industrial, and defense sectors. We believe that integrating the designed manipulator into robotic systems capable of performing diverse tasks has the potential to unlock broader possibilities and expand its functional scope.

The existing 3DOF spherical platform may be directly augmented with specially designed spherical roller bearings to yield enhanced performance. Furthermore, we plan to integrate haptic systems into the designed novel bio-inspired 3DOF SRM to provide more precise control [106,107], ensuring tactile and force feedback [108,109], which will contribute to achieving robust and stable control mechanisms [110]. We believe that the proposed methods for human–robot interaction, combined with advancements in AI technology and modern automation, will contribute significantly to the development of effective solutions in robotics.

Author Contributions: Conceptualization, S.S. and R.R.; methodology, S.S.; software, S.S.; validation, R.R.; formal analysis, S.S. and R.R.; investigation, S.S. and R.R.; resources, S.S.; data curation, S.S. and R.R.; writing—original draft preparation, S.S.; writing—review and editing, R.R.; visualization, S.S.; supervision, R.R. All authors have read and agreed to the published version of the manuscript.

Funding: This research was not supported by any external funding.

Data Availability Statement: The data are not publicly available at the time of publication because they are not in a format that is easily accessible or reusable by other researchers. However, the data supporting the findings of this study are archived and can be provided by the corresponding author upon reasonable request.

Acknowledgments: We extend our gratitude to Florida State University and its technical staff at the Digital Fabrication Lab (Fablab) for their invaluable support during the fabrication of the robotic system.

Conflicts of Interest: The authors declare no conflicts of interest.

References

1. Adams, C.R.; DeMartino, A.M.; Rego, G.; Denard, P.J.; Burkhart, S.S. The rotator cuff and the superior capsule: Why we need both. *Arthrosc. J. Arthrosc. Relat. Surg.* **2016**, *32*, 2628–2637. [CrossRef] [PubMed]
2. Bakhsh, W.; Nicandri, G. Anatomy and Physical Examination of the Shoulder. *Sports Med. Arthrosc. Rev.* **2018**, *26*, e10–e22. [CrossRef] [PubMed]
3. De Lange, A.; Kauer, J.M.; Huiskes, R. Kinematic behavior of the human wrist joint: A roentgen-stereophotogrammetric analysis. *J. Orthop. Res.* **1985**, *3*, 56–64. [CrossRef] [PubMed]
4. Han, L.; Cheng, L.; Li, H.; Zou, Y.; Qin, S.; Zhou, M. Hierarchical Optimization for Personalized Hand and Wrist Musculoskeletal Modeling and Motion Estimation. *IEEE Trans. Biomed. Eng.* **2025**, *72*, 454–465. [CrossRef]
5. Molini, L.; Precerutti, M.; Gervasio, A.; Draghi, F.; Bianchi, S. Hip: Anatomy and US technique. *J. Ultrasound* **2011**, *14*, 99–108. [CrossRef]
6. Kumar, S.; Mohanan, S.; Vattoth, A.L.; Bajaj, G.; Pandey, T. Anatomy and Biomechanics of Lower Extremity Tendons: Imaging Implications. *Semin. Ultrasound CT MRI* **2023**, *44*, 364–385. [CrossRef]
7. Brockett, C.L.; Chapman, G.J. Biomechanics of the ankle. *Orthop. Trauma* **2016**, *30*, 232–238. [CrossRef]
8. Pol, F.; Baharlouei, H.; Taheri, A.; Menz, H.B.; Forghany, S. Foot and ankle biomechanics during walking in older adults: A systematic review and meta-analysis of observational studies. *Gait Posture* **2021**, *89*, 14–24. [CrossRef]
9. Arias-Martorell, J. The morphology and evolutionary history of the glenohumeral joint of hominoids: A review. *Ecol. Evol.* **2019**, *9*, 703–722. [CrossRef]
10. Larson, S.G. Functional morphology of the shoulder in primates. In *Postcranial Adaptation in Nonhuman Primates*; Gebo, D.L., Ed.; Northern Illinois University Press: DeKalb, IL, USA, 1993; pp. 45–69.
11. Larson, S.G. New characters for the functional interpretation of primate scapulae and proximal humeri. *Am. J. Phys. Anthropol.* **1995**, *98*, 13–35. [CrossRef]
12. Evans, H.E.; de Lahunta, A. *Miller's Anatomy of the Dog, 4th ed*; Elsevier Saunders: St. Louis, MO, USA, 2012; p. 871.
13. Reis Silva, H.; Uosyte, R.; Clements, D.N.; Bergkvist, G.T.; Schwarz, T. Computed tomography and positive contrast computed tomographic arthrography of the canine shoulder: Normal anatomy and effects of limb position on visibility of soft tissue structures. *Vet. Radiol. Ultrasound* **2013**, *54*, 470–477. [CrossRef] [PubMed]
14. Manafzadeh, A.R. Joint mobility as a bridge between form and function. *J. Exp. Biol.* **2023**, *1*, 226. [CrossRef] [PubMed]
15. Bledt, G.; Powell, M.J.; Katz, B.; Di Carlo, J.; Wensing, P.M.; Kim, S. Mit cheetah 3: Design and control of a robust, dynamic quadruped robot. In Proceedings of the 2018 IEEE InRSJ International Conference on Intelligent Robots and Systems (IROS), Madrid, Spain, 1–5 October 2018; pp. 2245–2252.
16. Becker, J.; Emmanuel, M.; Jean-Marc, L. Joint loading estimation method for horse forelimb high jerk locomotion: Jumping. *J. Bionic Eng.* **2019**, *16*, 674–685. [CrossRef]
17. Böhmer, C.; Theil, J.C.; Fabre, A.C.; Herrel, A. *Atlas of Terrestrial Mammal Limbs*; CRC Press: Boca Raton, FL, USA, 2020.
18. Brocklehurst, R.J.; Fahn-Lai, P.; Regnault, S.; Pierce, S.E. Musculoskeletal modeling of sprawling and parasagittal forelimbs provides insight into synapsid postural transition. *iScience* **2022**, *25*, 103578. [CrossRef] [PubMed]
19. Gatesy, S.M.; Manafzadeh, A.R.; Bishop, P.J.; Turner, M.L.; Kambic, R.E.; Cuff, A.R.; Hutchinson, J.R. A proposed standard for quantifying 3-D hindlimb joint poses in living and extinct archosaurs. *J. Anat.* **2022**, *241*, 101–118. [CrossRef]
20. Kambic, R.E.; Roberts, T.J.; Gatesy, S.M. 3-D range of motion envelopes reveal interacting degrees of freedom in avian hind limb joints. *J. Anat.* **2017**, *231*, 906–920. [CrossRef]
21. Stowers, A.K.; Matloff, L.Y.; Lentink, D. How pigeons couple three-dimensional elbow and wrist motion to morph their wings. *J. R. Soc. Interface* **2017**, *14*, 20170224. [CrossRef]
22. Baier, D.B.; Gatesy, S.M.; Dial, K.P. Three-dimensional, high-resolution skeletal kinematics of the avian wing and shoulder during ascending flapping flight and uphill flap-running. *PLoS ONE* **2013**, *8*, e63982. [CrossRef]
23. Heers, A.M.; Baier, D.B.; Jackson, B.E.; Dial, K.P. Flapping before flight: High resolution, three-dimensional skeletal kinematics of wings and legs during avian development. *PLoS ONE* **2016**, *11*, e0153446. [CrossRef]
24. Lauder, G.V.; Tangorra, J.L. Fish locomotion: Biology and robotics of body and fin-based movements. *Robot. Fish: Bio-Inspired Fishlike Underw. Robot.* **2015**, 25–49.
25. Sudki, B.; Lauria, M.; Noca, F. Marine propulsor based on a three-degree-of-freedom actuated spherical joint. In Proceedings of the 3rd International Symposium on Marine Propulsors, Tasmania, Australia, 4 May 2013; pp. 481–485.
26. Cortés Torres, E.D.; García Gonzales, L.E.; Villamizar Marin, L.E.; García Cena, C.E. Mechanical Design of a New Hybrid 3R-DoF Bioinspired Robotic Fin Based on Kinematics Modeling and Analysis. *Actuators* **2024**, *13*, 353. [CrossRef]
27. Pandey, J.; Reddy, N.S.; Ray, R.; Shome, S.N. Biological swimming mechanism analysis and design of robotic frog. In Proceedings of the 2013 IEEE International Conference on Mechatronics and Automation, Takamatsu, Japan, 4 August 2013; pp. 1726–1731.
28. Torii, N.; Mizuno, H.; Iwasaki, K. Wrist Assembly for an Industrial Robot. U.S. Patent US 4,972,735, 27 November 1990.

29. Gosselin, C.M.; Hamel, J.F. The Agile Eye: A high-performance three-degree-of-freedom camera-orienting device. In Proceedings of the IEEE International Conference on Robotics and Automation, San Diego, CA, USA, 8–13 May 1994; Volume 1, p. 781.
30. Gosselin, C.M.; Pierre, E.S.; Gagne, M. On the development of the agile eye. *IEEE Robot. Autom. Mag.* **1996**, *3*, 29–37. [CrossRef]
31. Leguay-Durand, S.; Reboulet, C. Optimal design of a redundant spherical parallel manipulator. *Robotica* **1997**, *15*, 399–405. [CrossRef]
32. Vischer, P.; Clavel, R. Argos: A novel 3-DoF parallel wrist mechanism. *Int. J. Robot. Res.* **2000**, *19*, 5–11. [CrossRef]
33. Birglen, L.; Gosselin, C.; Pouliot, N.; Monsarrat, B.; Laliberté, T. SHaDe, a new 3-DOF haptic device. *IEEE Trans. Robot. Autom.* **2002**, *18*, 166–175. [CrossRef]
34. Lum, M.J.; Rosen, J.; Sinanan, M.N.; Hannaford, B. Optimization of a spherical mechanism for a minimally invasive surgical robot: Theoretical and experimental approaches. *IEEE Trans. Biomed. Eng.* **2006**, *53*, 1440–1445. [CrossRef]
35. Schuler, S.; Kaufmann, V.; Houghton, P.; Székely, G.S. Design and development of a joint for the dextrous robot arm. In Proceedings of the Ninth ESA Workshop on Advanced Space Technologies for Robotics and Automation, Noordwijk, The Netherlands, 28–30 November 2006; pp. 28–30.
36. Yu, Y.; Narita, Y.; Harada, Y.; Tsujio, S. Development of 3-DOF active rotational ball joint. In Proceedings of the 2007 IEEE International Conference on Robotics and Biomimetics (ROBIO), Sanya, China, 15–18 December 2007; pp. 1966–1971.
37. Hess-Coelho, T.A. A redundant parallel spherical mechanism for robotic wrist applications. *J. Mech. Des.* **2007**, *129*, 891–895. [CrossRef]
38. Inada, T.; Tsujimori, T.; Kitamura, S.; Taniuchi, R. Robot. U.S. Patent 7,622,001, granted on November 24, 2009.
39. Yu, Y.; Narita, Y.; Harada, Y.; Nakao, T. Research of 3-DOF active rotational ball joint. In Proceedings of the 2009 IEEE/RSJ International Conference on Intelligent Robots and Systems, St. Louis, MO, USA, 10 October 2009; pp. 5153–5158.
40. Wu, G.; Caro, S.; Bai, S.; Kepler, J. Dynamic modeling and design optimization of a 3-DOF spherical parallel manipulator. *Robot. Auton. Syst.* **2014**, *62*, 1377–1386. [CrossRef]
41. Degirmenci, A.; Hammond, F.L.; Gafford, J.B.; Walsh, C.J.; Wood, R.J.; Howe, R.D. Design and control of a parallel linkage wrist for robotic microsurgery. In Proceedings of the 2015 IEEE/RSJ International Conference on Intelligent Robots and Systems (IROS), Hamburg, Germany, 28 September 2015; pp. 222–228.
42. Sadeqi, S.; Bourgeois, S.P.; Park, E.J.; Arzanpour, S. Design and performance analysis of a 3-rrr spherical parallel manipulator for hip exoskeleton applications. *J. Rehabil. Assist. Technol. Eng.* **2017**, *4*, 2055668317697596. [CrossRef]
43. Lee, J.; Song, B.W.; Yang, W. Design of exoskeleton-type wrist human–machine interface based on over-actuated coaxial spherical parallel mechanism. *Adv. Mech. Eng.* **2018**, *10*, 1687814017753896. [CrossRef]
44. Li, X.; Liu, J.; Chen, W.; Bai, S. Integrated design, modeling and analysis of a novel spherical motion generator driven by electromagnetic principle. *Robot. Auton. Syst.* **2018**, *106*, 69–81. [CrossRef]
45. Bai, S.; Li, X.; Angeles, J. A review of spherical motion generation using either spherical parallel manipulators or spherical motors. *Mech. Mach. Theory* **2019**, *140*, 377–388. [CrossRef]
46. Hofer, M.; D'Andrea, R. Design, fabrication, modeling and control of a fabric-based spherical robotic arm. *Mechatronics* **2020**, *68*, 102369. [CrossRef]
47. Abe, K.; Tadakuma, K.; Tadakuma, R. ABENICS: Active ball joint mechanism with three-DoF based on spherical gear meshings. *IEEE Trans. Robot.* **2021**, *37*, 1806–1825. [CrossRef]
48. Rommers, J.; van der Wijk, V.; Herder, J.L. A new type of spherical flexure joint based on tetrahedron elements. *Precis. Eng.* **2021**, *71*, 130–140. [CrossRef]
49. Choi, D.; Kim, C.; Song, J.B. Development of microsurgical robot arm using spherical serial RCM mechanism and commercial laparoscopic surgical robot instrument. In Proceedings of the 2022 19th International Conference on Ubiquitous Robots (UR), Jeju, Korea, 4 July 2022; pp. 159–164.
50. Howard, I.S. Design and kinematic analysis of a 3D-printed 3DOF robotic manipulandum. In *Annual Conference Towards Autonomous Robotic Systems*; Springer: Berlin/Heidelberg, Germany, 2013; pp. 227–239.
51. Ghaedrahmati, R.; Gosselin, C. Kinematic Analysis of a New 3-DOF Parallel Wrist-Gripper Assembly with a Large Singularity-Free Workspace. *Actuators* **2023**, *12*, 421. [CrossRef]
52. Zhang, P.; Deng, Z.; Hou, X.; Wang, S. Development of a miniaturized bedside robotic wrist with multifunctional movement capabilities: An analysis based on a simulation environment. In Proceedings of the 2023 IEEE 3rd International Conference on Digital Twins and Parallel Intelligence (DTPI), Orlando, FL, USA, 7 November 2023; pp. 1–5.
53. Schröder, K.; Garcia, G.; Chacón, R.; Montenegro, G.; Marroquín, A.; Farias, G.; Dormido-Canto, S.; Fabregas, E. Development and control of a real spherical robot. *Sensors* **2023**, *23*, 3895. [CrossRef]
54. Djennane, M.; Chehaidia, S.E.; Yakoub, C.; Mesbah, K.; Aljohani, M.; Mosaad, M.I. Design, Analysis and Implementation of a 3-DOF Spherical Parallel Manipulator. *IEEE Access* **2024**, *12*, 52837–52850. [CrossRef]
55. Zhang, L.; Yu, Z.; Su, P.; Li, J.; Ge, R. Design of a Parallel Wrist Rehabilitation Robot and Analysis of Physiological Effect on Training. *IEEE/ASME Trans. Mechatron.* **2024**, *29*, 3401–3414. [CrossRef]

56. Zhang, P.; Deng, Z.; Hou, X.; Wang, S. Development of a Parallel-Mechanism-Based Robotic Wrist With Remote Center of Motion Capability to Assist Ultrasound Scanning. *IEEE J. Radio Freq. Identif.* **2024**, *8*, 341–347. [CrossRef]
57. Krebs, H.I.; Volpe, B.T.; Williams, D.; Celestino, J.; Charles, S.K.; Lynch, D.; Hogan, N. Robot-aided neurorehabilitation: A robot for wrist rehabilitation. *IEEE Trans. Neural Syst. Rehabil. Eng.* **2007**, *15*, 327–335. [CrossRef] [PubMed]
58. Pehlivan, A.U.; Sergi, F.; Erwin, A.; Yozbatiran, N.; Francisco, G.E.; O'Malley, M.K. Design and validation of the RiceWrist-S exoskeleton for robotic rehabilitation after incomplete spinal cord injury. *Robotica* **2014**, *32*, 1415–1431. [CrossRef]
59. Fite, K.B.; Withrow, T.J.; Shen, X.; Wait, K.W.; Mitchell, J.E.; Goldfarb, M. A gas-actuated anthropomorphic prosthesis for transhumeral amputees. *IEEE Trans. Robot.* **2008**, *24*, 159–169. [CrossRef]
60. Fan, S.; Fan, S.; Jiang, L.; Liu, H. A design of a miniaturized prosthetic wrist based on repetition rate of human wrist daily tasks. In Proceedings of the 2016 IEEE International Conference on Robotics and Biomimetics (ROBIO), Qingdao, China, 3 December 2016; pp. 1643–1648.
61. Amirabdollahian, F.; Ates, S.; Basteris, A.; Cesario, A.; Buurke, J.; Hermens, H.; Hofs, D.; Johansson, E.; Mountain, G.; Nasr, N.; et al. Design, development and deployment of a hand/wrist exoskeleton for home-based rehabilitation after stroke-SCRIPT project. *Robotica* **2014**, *32*, 1331–1346. [CrossRef]
62. Singh, N.; Saini, M.; Anand, S.; Kumar, N.; Srivastava, M.P.; Mehndiratta, A. Robotic exoskeleton for wrist and fingers joint in post-stroke neuro-rehabilitation for low-resource settings. *IEEE Trans. Neural Syst. Rehabil. Eng.* **2019**, *27*, 2369–2377. [CrossRef]
63. Jarrassé, N.; Tagliabue, M.; Robertson, J.V.; Maiza, A.; Crocher, V.; Roby-Brami, A.; Morel, G. A methodology to quantify alterations in human upper limb movement during co-manipulation with an exoskeleton. *IEEE Trans. Neural Syst. Rehabil. Eng.* **2010**, *18*, 389–397. [CrossRef]
64. Rose, C.G.; Sergi, F.; Yun, Y.; Madden, K.; Deshpande, A.D.; O'Malley, M.K. Characterization of a hand-wrist exoskeleton, READAPT, via kinematic analysis of redundant pointing tasks. In Proceedings of the 2015 IEEE International Conference on Rehabilitation Robotics (ICORR), Singapore, 11 August 2015; pp. 205–210.
65. Pezent, E.; Rose, C.G.; Deshpande, A.D.; O'Malley, M.K. Design and characterization of the Open Wrist: A robotic wrist exoskeleton for coordinated hand-wrist rehabilitation. In Proceedings of the 2017 International Conference on Rehabilitation Robotics (ICORR), London, UK, 17 July 2017; pp. 720–725.
66. Bajaj, N.M.; Spiers, A.J.; Dollar, A.M. State of the art in artificial wrists: A review of prosthetic and robotic wrist design. *IEEE Trans. Robot.* **2019**, *35*, 261–277. [CrossRef]
67. Li, J.; Zuo, S.; Zhang, L.; Dong, M.; Zhang, Z.; Tao, C.; Ji, R. Mechanical design and performance analysis of a novel parallel robot for ankle rehabilitation. *J. Mech. Robot.* **2020**, *12*, 051007. [CrossRef]
68. Vertongen, J.; Kamper, D.G.; Smit, G.; Vallery, H. Mechanical aspects of robot hands, active hand orthoses, and prostheses: A comparative review. *IEEE/ASME Trans. Mechatron.* **2020**, *926*, 955–965. [CrossRef]
69. Eschweiler, J.; Li, J.; Quack, V.; Rath, B.; Baroncini, A.; Hildebrand, F.; Migliorini, F. Anatomy, biomechanics, and loads of the wrist joint. *Life* **2022**, *12*, 188. [CrossRef]
70. Soltanov, S. Structural synthesis of the robot manipulators with general constraint one using the transformation of the higher kinematic pare. *Mechanics* **2020**, *39*, 37–43.
71. Alizade, R.; Soltanov, S.; Hamidov, A. Structural synthesis of lower-class robot manipulators with general constraint one. *Robotics* **2021**, *10*, 14. [CrossRef]
72. Soltanov, S. Structural synthesis of the new type 4DOF robot manipulators for industry and medicine. *Aust. J. Mech. Eng.* **2023**, *22*, 911–923. [CrossRef]
73. Yousaf, R.; Shahzad, A.; Qadri, M.M.; Javed, A. Recent advancements in flapping mechanism and wing design of micro aerial vehicles. *Proc. Inst. Mech. Eng. Part C: J. Mech. Eng. Sci.* **2021**, *235*, 4425–4446. [CrossRef]
74. Amal, P.; Nair, A.R.; Arunav, H.; Raj, R.; Akhil, V.M.; Tawk, C.; Shankar, K.V. Bioinspiration and biomimetics in marine robotics: A review on current applications and future trends. *Bioinspiration Biomim.* **2024**, *19*, 031002.
75. Morgansen, K.A.; Triplett, B.I.; Klein, D.J. Geometric methods for modeling and control of free-swimming fin-actuated underwater vehicles. *IEEE Trans. Robot.* **2007**, *23*, 1184–1199. [CrossRef]
76. Kim, H.J.; Song, S.H.; Ahn, S.H. A turtle-like swimming robot using a smart soft composite (SSC) structure. *Smart Mater. Struct.* **2012**, *22*, 014007. [CrossRef]
77. Li, B.; Li, Z.; Li, H.; Du, Y. Optimization of Three-Degree-of-Freedom Biomimetic Pectoral Fin Propulsion Law. *J. Shanghai Jiaotong Univ. (Sci.)* **2024**, *24*, 1–4. [CrossRef]
78. Wyrobek, K.A.; Berger, E.H.; Van der Loos, H.M.; Salisbury, J.K. Towards a personal robotics development platform: Rationale and design of an intrinsically safe personal robot. In Proceedings of the 2008 IEEE International Conference on Robotics and Automation, Pasadena, CA, USA, 19 May 2008; pp. 2165–2170.
79. Mahmoud, R.A.; Ueno, A.; Tatsumi, S. An assistive tele-operated anthropomorphic robot hand: Osaka city university hand ii. In Proceedings of the 6th International Conference on Human-Robot Interaction, New York, NY, USA, 6–9 March 2011; pp. 85–92.

80. Chernyak, V.; Flynn, T.; O'Rourke, J.; Morgan, J.; Zalutsky, A.; Chernova, S.; Nestinger, S.S.; Padir, T. The design and realization of a high mobility biomimetic quadrupedal robot. In Proceedings of the 2012 IEEE/ASME 8th IEEE/ASME International Conference on Mechatronic and Embedded Systems and Applications, Suzhou, China, 8–10 July 2012; pp. 93–98.
81. Bright, D.; Shield, S.; Patel, A. AeroDima: Cheetah-Inspired Aerodynamic Tail Design for Rapid Maneuverability. In Proceedings of the 2024 IEEE International Conference on Robotics and Automation (ICRA), Yokohama, Japan, 13–17 May 2024; pp. 1451–1456.
82. Hammond, F.L.; Howe, R.D.; Wood, R.J. Dexterous high-precision robotic wrist for micromanipulation. In Proceedings of the 2013 16th International Conference on Advanced Robotics (ICAR), Montevideo, Uruguay, 25–29 November 2013; pp. 1–8.
83. Hu, T.; Lu, X.; Yi, J.; Wang, Y.; Xu, D. Biomimetic soft robotic wrist with 3-DOF motion and stiffness tunability based on ring-reinforced pneumatic actuators and a particle jamming joint. *Sci. China Technol. Sci.* **2024**, *67*, 774–790. [CrossRef]
84. Hwang, Y.H.; Kang, S.R.; Cha, S.W.; Choi, S.B. An electrorheological spherical joint actuator for a haptic master with application to robot-assisted cutting surgery. *Sens. Actuators A Phys.* **2016**, *249*, 163–171. [CrossRef]
85. Hernández-Flores, E.A.; Hernández-Rodríguez, Y.M.; Munguía-Fuentes, R.; Bayareh-Mancilla, R.; Cigarroa-Mayorga, O.E. Acinonyx jubatus-Inspired Quadruped Robotics: Integrating Neural Oscillators for Enhanced Locomotion Control. *Biomimetics* **2024**, *9*, 318. [CrossRef] [PubMed]
86. Kuka AG. Augsburg, Germany. 2017. Available online: www.kuka.com (accessed on 3 December 2024).
87. Selvamuthu, M.G.; Abe, K.; Tadakuma, K.; Tadakuma, R. Metal ABENICS: Metallic Spherical Gear Mechanism with Orientation Correction using Embedded IMU Sensor. In Proceedings of the 2024 IEEE International Conference on Advanced Intelligent Mechatronics (AIM), Boston, MA, USA, 15–18 July 2024; pp. 256–263.
88. *Human Factors Engineering*, 3rd ed.; McCormick, E.J., Ed.; McGraw-Hill: New York, NY, USA, 1970.
89. Rosenbaum, D.A.; Jorgensen, M.J. Planning macroscopic aspects of manual control. *Hum. Mov. Sci.* **1992**, *11*, 61–69. [CrossRef]
90. Chan, W.P.; Parker, C.A.; Van der Loos, H.M.; Croft, E.A. Grip forces and load forces in handovers: Implications for designing human-robot handover controllers. In Proceedings of the Proceedings of the Seventh Annual ACM/IEEE International Conference on Human-Robot Interaction, Boston, MA, USA, 5–8 March 2012; pp. 9–16.
91. Jeannerod, M. The timing of natural prehension movements. *J. Mot. Behav.* **1984**, *16*, 235–254. [CrossRef] [PubMed]
92. Zwicker, J.G.; Missiuna, C.; Harris, S.R.; Boyd, L.A. Developmental coordination disorder: A review and update. *Eur. J. Paediatr. Neurol.* **2012**, *16*, 573–581. [CrossRef] [PubMed]
93. Goldstein, H.; Pool, C.; Safko, J. *Classical Mechanics*, 3rd ed.; Pearson: Miami, FL, USA, 2001.
94. Courant, R.; Robbins, H.; Stewart, I. *What is Mathematics, Euler's Formula*; Oxford University Press: New York, NY, USA, 1996; pp. 235–240.
95. Kutzbach, K. Mechanische leitungsverzweigung, ihre gezetze und anwendungen, Maschinenbau. *Der Betr.* **1929**, *8*, 710–716.
96. Ceccarelli, M. Screw axis defined by Giulio Mozzi in 1763 and early studies on helicoidal motion. *Mech. Mach. Theory* **2000**, *35*, 761–770. [CrossRef]
97. Brockett, R. Robotic manipulators and the product of exponential formula. In *Mathematical Theory of Networks and Systems*; Fuhrman, P.A., Ed.; Springer: New York, NY, USA, 1984; pp. 120–129.
98. Levenberg, K. A method for the solution of certain problems in least squares. *Quart. Appl. Math.* **1944**, *2*, 164–168.
99. Marquardt, D. An algorithm for least-squares estimation of nonlinear parameters. *SIAM J. Appl. Math.* **1963**, *11*, 431–441. [CrossRef]
100. Lynch, K.M.; Park, F.C. *Modern Robotics: Mechanics, Planning, and Control*; Cambridge University Press: Cambridge, UK, 2017; ISBN 9781107156302.
101. Ohkawa, T.; He, K.; Sener, F.; Hodan, T.; Tran, L.; Keskin, C. Assemblyhands: Towards egocentric activity understanding via 3d hand pose estimation. In Proceedings of the IEEE/CVF Conference on Computer Vision and Pattern Recognition, Vancouver, BC, Canada, 17–24 June 2023; pp. 12999–13008.
102. Zhao, T.Z.; Kumar, V.; Levine, S.; Finn, C. Learning fine-grained bimanual manipulation with low-cost hardware. *arXiv* **2023**, arXiv:2304.13705.
103. Wu, P.; Shentu, Y.; Yi, Z.; Lin, X.; Abbeel, P. Gello: A general, low-cost, and intuitive teleoperation framework for robot manipulators. *arXiv* **2023**, arXiv:2309.13037.
104. Wang, C.; Shi, H.; Wang, W.; Zhang, R.; Fei-Fei, L.; Liu, C.K. Dexcap: Scalable and portable mocap data collection system for dexterous manipulation. *arXiv* **2024**, arXiv:2403.07788.
105. Qin, Y.; Yang, W.; Huang, B.; Van Wyk, K.; Su, H.; Wang, X.; Chao, Y.W.; Fox, D. Anyteleop: A general vision-based dexterous robot arm-hand teleoperation system. *arXiv* **2023**, arXiv:2307.04577.
106. Gillespie, R.B.; Colgate, J.E.; Peshkin, M.A. A general framework for cobot control. *IEEE Trans. Robot. Autom.* **2001**, *17*, 391–401. [CrossRef]
107. Moore, C.A.; Peshkin, M.A.; Colgate, J.E. Cobot implementation of virtual paths and 3D virtual surfaces. *IEEE Trans. Robot. Autom.* **2003**, *19*, 347–351. [CrossRef]

108. Colgate, J.E.; Brown, J.M. Factors affecting the z-width of a haptic display. In Proceedings of the 1994 IEEE International Conference on Robotics and Automation, San Diego, CA, USA, 8–13 May 1994; pp. 3205–3210.
109. Faulring, E.L.; Lynch, K.M.; Colgate, J.E.; Peshkin, M.A. Haptic display of constrained dynamic systems via admittance displays. *IEEE Trans. Robot.* **2007**, *23*, 101–111. [CrossRef]
110. Roberts, R.G.; Moore, C.A.; Colgate, J.E. A New Expression for the Passivity Bound for a Class of Sampled-Data Systems. *IEEE Trans. Robot.* **2024**, *40*, 4179–4189. [CrossRef]